Institute for Theoretical Physics, Utrecht University.

An Investigation of Microfluidic Transport Through Ionic Channels

MASTER'S THESIS

Dónal James McGrath
Theoretical Physics

Supervisor:
Prof. Dr. René VAN ROIJ
Institute for Theoretical Physics
Daily Supervisor:
MSc. Tim KAMSMA
Institute for Theoretical Physics
Secondary Supervisor:
Dr. Joost DE GRAAF
Institute for Theoretical Physics

31 January 2024

Acknowledgements

During the course of this thesis, there have been many ups and downs, to say the least. There have been so many people who were there for me and provided necessary distractions when researching. I would like to thank as many as I possibly can. I would like to thank my supervisor René, you have inspired me to keep investigating this topic with your endless enthusiasm. To my daily supervisor Tim, thank you for always helping out with the many COMSOL shenanigans along with providing very useful insights into microfluidic channels. For any question I had both of you were able to answer me with amazing detail and in a manner that made it easy to understand. To Alexander, thank you for helping me by asking questions at our weekly presentations.

To my family, Mary, Brendan, Aoife and Enda. Thank you for always picking up the phone when I needed you. I wouldn't be where I am today without your constant words of encouragement and thoughtful insights. To my physics friends from "Riley's Crew", Riley, Eline, Monica, Sjoerd, Robert, Teun and Mithuss. Thank you all for being amazing friends, I will always be grateful for your help throughout this master's along with our frequent walks around the campus and occasional dinner parties. You made this master's an incredibly fun time. To the "Basta broscetta's", Alessia, Sem, Roos, Bas, Zoë and Jurriaan thank you all for our frequent dinners and parties in general, you all have been great colleagues but most importantly great friends throughout this masters. To my friends from my bachelor's in Galway, Mario, Emmmet, Conor, Griffen and Daniel. You all have been my closest friends for many years and I am delighted that each of you has kept in contact despite the distance. To the "Wild Cones", Patrick, Adrian and Darren. It has been fantastic being around you guys even though each of us is now in different places we all manage to meet up semi-regularly. This has always been a welcome distraction but also a fantastic excuse to talk maths and reminisce on funny stories throughout my thesis. To Kruthika thank you for being a great friend and meeting up for a coffee every now and then, it has always been really nice to talk to you ever since we first met as housemates of 169 Warande.

Finally, I would like to thank Gina Dowd and Gülsüm Öztürk. You both have guided me and were always there to help. I am ever so thankful. To the nameless volunteer in Galway, I will be forever grateful to you.

Abstract

Memristors have been propelled into the scientific consciousness in recent decades due to their applications in neuromorphic computations. Memristors are resistors with memory, a history-dependent electrical device predicted by Chua in the 1970s as the missing fourth passive circuit element on the basis of symmetry. The first memristive devices were discovered in 2012 in semiconductor solid-state devices. Recently, our research group predicted the memristive capabilities of microfluidic systems containing an aqueous electrolyte in a cone-shaped channel [19], such iontronic devices can perform computing tasks [20]. The theoretical model for these systems is developed from the Poisson-Nernst-Planck-Stokes equation, where we extend these studies to include bipolar cylindrical and conical channels, rather than unipolar channels which has been at the forefront of current research. This model is used to understand the effect of changing geometries for an applied steady-state voltage. The analytical model successfully provides accurate predictions of Ohmic and Diodic electric current behaviour that we can attribute to salt accumulation or depletion in the channel due to an applied static electric potential drop over the channel. Moreover, we consider the volumetric electro-osmotic fluid flow upon an electric driving force, a phenomenon that has no alternative in solid-state systems. To test the accuracy of the model we compare it to finite element calculations, revealing that the electric current behaviour in both geometries has been successfully predicted, but for the volumetric flow, only the cylindrical channel matches well with finite element calculations. Further research into the effects of geometry in ionic channels is encouraged to understand memristive behaviour.

Contents

1 Introduction

1.1 The History of Memristors

There are three well-known passive classical circuit elements, the resistor (relating voltage and current), the inductor (relating magnetic flux and current), and lastly, the capacitor (relating charge and voltage). However, there is still one possible relationship undefined, that of relating the charge and magnetic flux. Thus, purely based on symmetry and completeness the memristor was theorised [6]. The term memristor is an amalgamation of *mem*ory and res*istor*. This fundamentally means that the resistance depends on the past states of the system and is the epitome of Chua's postulate in 1971 [6]. In 1976, Chua extrapolated the original concept into a broader generalisation of memristive systems [8], we will discuss this further in later sections. This sparked the phrase "if it's pinched, it's a memristor" [7], which refers to a current-voltage diagram in which a pinched-hysteresis loop is generated in the case that a memristor is being studied with a time-dependant voltage. This pinched-hysteresis loop, originally described as Lissajous figures where the pinch passes through the origin, serves as a simple but effective authentication of memristive devices [28].

Chua developed the theory of memristance as a mathematical description therefore, it was not a recipe for creating memristors. However, it can be noted that most memristors were created unintentionally. The first recorded memristor to be created artificially was Sir Humphrey Davy's arc lamp, created in 1801 [4, 10, 31]. The arc lamp bore the hallmark essence of memristors, Lissajous figures pinched at the origin which was discovered through experiments on discharge tubes in 1948 [12]. These lamps used thin oxide films attached to a power supply to create light. Such memristors which require an active non-passive power supply to create a memristive effect are known as volatile. An interesting point to note is that a memristor can be passive, meaning that an active non-passive power supply is not needed, at the time when they were theorised it was most assumed it would be unachievable and would have no practical significance.

This remained the consensus for thirty years until interest was sparked in 2008 when HP developed a titanium oxide memristor [43]. This was the first instance of a non-volatile memristor, experiments produced a two-terminal memristor measuring less than 50 nm in diameter which ignited interest both commercially and in academia. For the first time, non-volatile memristors now appeared to be experimentally achievable.

1.2 Iontronic Devices

The focus of this thesis surrounds iontronic devices. Iontronic devices are electronic devices which use ions dissolved in water to, for example, transmit, store and generate signals [30]. These devices became propelled into the consciousness of soft matter research in 2010 when a book titled 'Iontronics' was published [24]. While ions transmit information slower than an electron due to the mode of transport being that of diffusivity [18,45]. This means that unfortunately, iontronic devices cannot compete with standard electronic devices in terms of speed. However, these devices use in theory the same mechanisms that are used within our brains [42]. Therefore, the potential of coupling these devices to biological systems has grown curiosity within the field in recent decades.

One important element which is present within both electronic and ionic devices is memory [25]. The most interesting memory device which we have briefly described earlier in this introduction is that of a memristor, a truly fascinating aspect of the biological nature of neuron communication is that it is considered to be a memristor. Therefore, these memory devices pose a fascinating way to understand the biological nature of our brains with physical models which replicate the responses of synaptic neurons [1]. Where a synaptic neuron is a core structure in the brain which is responsible for receiving sensory information, and sending a response to the stimulus [36]. Modelling a complex process such as the brain poses many problems but by focusing on specific aspects of the system as seen in Figure 18(a), where there is a surface charge along the length of the channel and a liquid electrolyte flowing laterally through the system we can understand the many unknowns posed by current research in synaptic neurons [39]. We aim in this thesis to understand how the liquid electrolyte flows through an iontronic device giving insight into the nature of information transmission. We will be researching two devices in particular that of a cylindrical channel, due to its symmetric geometry we can use this as a basis to understand the complex nature of the flow to propel us to the next more complex system, that of a conical channel. As the conical channel has an asymmetric geometry due to the base and tip radii being different the fluid flow becomes more complex. The methods we will use to achieve this are a combination of numerical and analytical analysis. The numerical analysis will be completed with the use of a powerful simulation software known as COMSOL through a method known as finite element analysis (FE), we will then compare this to an analytical approximation (AA). The analytical side of this thesis will combine several equations which couple the electrostatic nature to the flow of the channel with an induced surface charge.

In Section 2 we will more concretely describe what a memristor and an iontronic device are by delving into the mathematical description of these systems. In Section 3 we will look at the specific case of a cylindrical channel with an electric potential drop across the channel and a surface charge density on the walls of the cylinder. We aim to create a set of equations which describe the system in full. We will then using these equations explore the nature of the volumetric fluid flow and the diodic nature as well as the time-dependent voltage. Furthering this we will in Section 5 investigate the volume flow of the conical channel as a special case, and we will also probe the diodic behaviour of the channel.

2 Theory of Memristors and Ionic Channels

2.1 A Brief Outlook

In this section, we will delve into the theory of memristors and ionic channels. This introduction will allow us to grasp the concepts which will arise in later sections. There are three main concepts which we aspire to gain an understanding of, memristors, how an electric double layer (EDL) forms and its properties, and lastly how a fluid is transported while being in contact with an EDL.

2.2 Memristor Theory

As briefly hinted at in our introduction memristors were originally theorized by L.Chua based on symmetry [6]. However, to give more context to what we mean by symmetry, observe in Fig (1) we have classical circuitry equations, namely that of induction L (yellow), resistance R (red), and capacitance C (blue), along with voltage current, charge, and flux denoted by V, I, q, and ϕ, respectively. The defined relationships as depicted in Fig 1 of voltage and current, flux and current, and charge and current. The undefined relationship is that

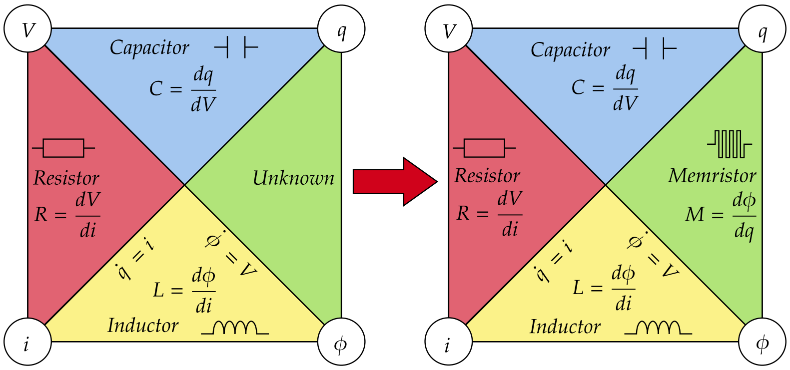

Figure 1: We have three known passive circuit elements, a resistor (red), an inductor (yellow), and a capacitor (blue) along with their associated differential equations. We define the following variables; voltage V, current i, charge q, and flux ϕ. From this pictorial view of circuit elements, we can note that if one differentiates the variables labelled in white, we obtain a function [4]. Chua theorized due to this that if one differentiates flux ϕ concerning charge q we arrive at a function which Chua calls memristance due to the dimensionality of M being that of resistance [6, 8].

of charge and flux. Two additional relationships, not mentioned thus far are represented along the diagonals

$$q(t) = \int_{-\infty}^{t} i(\tau)\,\mathrm{d}\tau \implies \dot{q}(t) = i(t), \tag{2.1}$$

$$\phi(t) = \int_{-\infty}^{t} V(\tau)\,\mathrm{d}\tau \implies \dot{\phi}(t) = V(t). \tag{2.2}$$

This culmination of information provides a nonlinear resistor, which provides a fascinating dependence on the memory of the device's previous state described in differential form as

$$\frac{V(t)}{i(t)} = \frac{\dot{\phi}}{\dot{q}} = \frac{d\phi}{dq} = M(q) = M\left(\int_{-\infty}^{t} i(\tau)\,\mathrm{d}\tau\right). \tag{2.3}$$

$M(q)$, known as memristance, has the unit of Ohm [6–8, 40]. The behaviour of a memristor is that of a non-linear resistor. However, to be classified as a memristor the device must have a pinched hysteresis loop that crosses at the origin. Hysteresis loops are associated with classical memory storage systems due to the dependence on the system's previous states [7].

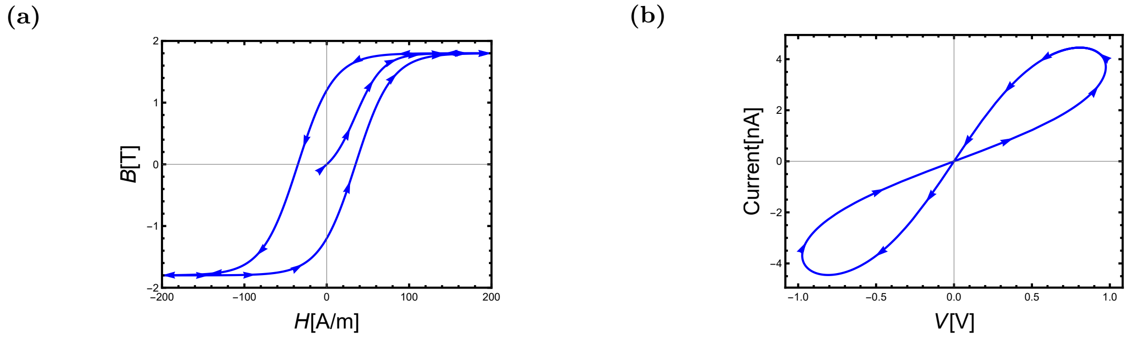

Figure 2: (a) Classical depiction of a magnetic hysteresis loop [44]. The arrows denote the direction of the system's next states until it reaches a plateau which means that the system's spins are aligned. **(b)** This is a Lissajous figure which depicts a self-crossing hysteresis loop. In a similar manner to the magnetic hysteresis loop, the memristor relies upon the previous states to form the loop denoted by the arrows [28].

The best-known example of a hysteresis loop is found in the magnetisation curve $B(H)$ of a magnet, Figure 2(a) depicts such a hysteresis loop where the magnetisation of the ferromagnetic depends on the history of the applied magnetic field H [44]. This phenomenon occurs due to there being multiple magnetic moments for a given applied magnetic field. In Figure 2(b), we show a different form of the hysteresis loop, one caused by memristance, a non-linear resistance creating an intersection point at the origin. To create such a diagram we apply a time-dependent periodic electric potential $V(t)$ and use the previous states indicated by the arrows in Figure 2(b). One can note that for high-frequency electric potentials, at the limit where the frequency approaches infinity, a memristive device will no longer have a pinched hysteresis loop but instead have an Ohmic current-voltage diagram, meaning linear resistance. This occurs due to the device being unable to adapt to its previous state, thus becoming an Ohmic resistor. If we consider low-frequency electric potentials we will observe non-linear resistance, this arises due to the device being able to equilibrate to the instantaneous potential.

So far we have purely discussed memristors. However, there are other devices which have memristor-like properties. Such devices have been designated as memristive systems. Chua defines these systems by

$$\frac{d\mathbf{x}}{dt} = f(\mathbf{x}, u, t), \tag{2.4}$$

$$y = g(\mathbf{x}, u, t)u, \tag{2.5}$$

where $\mathbf{x}$ is a vector of the internal states of the system, u denotes the input and y is the output of the system [8]. The physical quantities which are generally associated with u and y are voltage and current respectively, a memristive system, or current-voltage, a memductive system. The function f is a continuous n-dimensional vector function and g is a continuous scalar function that is monotonic in u and is bounded. Now we arrive at the hallmark property of a memristive system that distinguishes a memristor from any other dynamical system: the pinched hysteresis loop where $u = 0 \Rightarrow y = 0$.

We have primarily discussed memristive systems in a general manner. However, throughout this thesis, we will only be discussing voltage-controlled memristors. Thus, if we alter Eq. (2.4) and Eq. (2.5) we arrive at the equations which will contribute to describing our iontronic system,

$$\frac{d\mathbf{x}}{dt} = f(\mathbf{x}, V, t), \tag{2.6}$$

$$I = G(\mathbf{x}, V, t)V(t). \tag{2.7}$$

Here we replaced u and y with electric potential V and current I, respectively. G is similarly defined as g from Eq. (2.5), and known as memductance with units of Siemens (S). Memductance is a contraction of memory and conductance. For an ideal voltage-controlled memristor, the memductance is dependent on the electric flux of the system and is then described by

$$\frac{d\phi}{dt} = V, \tag{2.8}$$

$$I = G(\phi)V(t), \tag{2.9}$$

where $\dot{\mathbf{x}} = \phi$ is the electric flux and

$$G(\phi) = \frac{dq}{d\phi}. \tag{2.10}$$

This concludes our discussion on the theory behind memristive devices.

2.3 The Electric Double Layer

We will be using Ref. [45] to aid in our understanding of electric double layers. Consider one charged plane, in contact with a 1:1 liquid electrolyte. We assume that this charged surface is translationally invariant in the x-y plane. An electric double layer (EDL) forms on the surface of a plane that has an induced charge applied to it while being in contact with a liquid electrolyte forming a diffusive layer of typical thickness given by the Debye length,

$$\lambda_D = \kappa^{-1} = \sqrt{\frac{\varepsilon k_B T}{e^2 \sum_i z_i^2 \rho_{i,b}}} = \sqrt{\frac{\varepsilon k_B T}{2\rho_b e^2}}, \tag{2.11}$$

where $\varepsilon = \epsilon_0 \epsilon_r$ is the electric permittivity described by ϵ_0 the vacuum permittivity accompanied with the relative dielectric constant ϵ_r, $k_B T$ the Boltzmann constant multiplied by the temperature of the system respectively, e is the elementary electric charge, z_i is the valency which denotes the charge sign of the ion, and lastly, the $\rho_{i,b}$ the bulk concentrations, respectively, i denotes the species of ions and b refers to the bulk.

The structure of the EDL arises from the Poisson-Boltzmann equation. This equation couples the Poisson equation for electrostatics with the Boltzmann distribution for ionic species. We can form a closed set of equations for the electric potential $\psi(\mathbf{r})$ and ion concentrations $\rho_i(\mathbf{r})$ with a charge $Q(\mathbf{r})$ acting on the system, providing we impose the relevant boundary conditions. The Poisson equation

$$\nabla^2 \psi(\mathbf{r}) = -\frac{Q(\mathbf{r})}{\varepsilon}, \tag{2.12}$$

with $Q(\mathbf{r}) = Q_{ext}(\mathbf{r}) + e\sum_i z_i \rho_i(\mathbf{r})$ the total charge density with $Q(\mathbf{r})$ composed of the surface charge density applied externally accompanied with the ionic charge density. We can simplify this relation by noting there is no surface charge density applied to the bulk, this will be accounted for in the boundary conditions, therefore, our equation reduces to $Q(\mathbf{r}) = e\sum_i z_i\rho_i(\mathbf{r}) = e(\rho_+(\mathbf{r}) - \rho_-(\mathbf{r})) = e\rho_e$, where ρ_e is the ionic space charge density for a 1:1 liquid electrolyte. Now we apply this to Eq. (2.12),

$$\nabla^2\psi(\mathbf{r}) = -\frac{e(\rho_+(\mathbf{r}) - \rho_-(\mathbf{r}))}{\varepsilon} = -\frac{e\rho_e}{\varepsilon}. \tag{2.13}$$

We aim to link the Poisson equation (2.13) with the Boltzmann equation for ionic concentrations,

$$\rho_i(\mathbf{r}) = \rho_{i,b}e^{-\frac{z_i e\psi(\mathbf{r})}{k_BT}}. \tag{2.14}$$

Combining (2.13) and (2.14) we form the Poisson-Boltzmann equation,

$$\nabla^2\psi(\mathbf{r}) = -\frac{e\left(\rho_{+,b}e^{-\frac{e\psi(\mathbf{r})}{k_BT}} - \rho_{-,b}e^{+\frac{e\psi(\mathbf{r})}{k_BT}}\right)}{\varepsilon}. \tag{2.15}$$

As our system is a 1:1 liquid electrolyte we impose bulk neutrality: $\rho_{+,b} = \rho_{-,b} = \rho_b$. Therefore, in a planar geometry Eq. (2.16) reduces to,

$$\frac{d^2\psi(z)}{dz^2} = \frac{2e\rho_b}{\varepsilon}\sinh\left(\frac{e\psi(z)}{k_BT}\right), \tag{2.16}$$

where we noted that our system is only dependent on the component in the z direction. To solve this equation we can simplify by substituting in a dimensionless electric potential $\phi(z) = e\psi(z)/k_BT$,

$$\frac{d^2\phi(z)}{dz^2} = \kappa^2\sinh\left(\phi(z)\right). \tag{2.17}$$

Here we used the Debye length (2.11). To solve Eq. (2.17) we can note that $\rho_\pm(z\to\infty) = \rho_b$ gives us a boundary condition for electrostatic potential,

$$\lim_{z\longrightarrow\infty}\psi(z) = 0. \tag{2.18}$$

Another boundary condition is that of global charge neutrality. The overall ionic charge is the direct opposite of that of the total surface charge. This leads us to

$$\begin{aligned}\sigma &= -\int_0^\infty \mathrm{d}zQ(z),\\ &= \frac{\varepsilon}{e}\int_0^\infty \mathrm{d}z\nabla^2\psi(z),\\ &= -\frac{\varepsilon}{e}\frac{d\psi}{dz}(0^+).\end{aligned} \tag{2.19}$$

Collecting the three boundary conditions and making them dimensionless we have:

$$\frac{d^2\phi(z)}{dz^2} = \kappa^2\sinh(\phi(z)), \tag{2.20}$$

$$\phi(z\to\infty) = 0, \tag{2.21}$$

$$\frac{d\phi}{dz}(0^+) = -\frac{e^2}{\varepsilon\varepsilon_0 k_BT}\sigma = -4\pi\lambda_B\sigma. \tag{2.22}$$

We introduced the constant

$$\lambda_B = \frac{e^2}{4\pi\epsilon\epsilon_0 k_BT},$$

formally known as the Bjerrum length, which describes the length of separation where the electrostatic interaction between two electric charges e is equal to the thermal energy scale and is a property of a solvent. The Bjerrum length is used as a coupling parameter in this theory due to it setting the strength of interactions and for water at room temperature $\lambda_B = 0.72$ nm.

The Poisson-Boltzmann Eqs. (2.20)-(2.22) can be solved analytically to give the dimensionless potential

$$\phi(z) = 2\ln\left(\frac{1+\gamma e^{-\kappa z}}{1-\gamma e^{-\kappa z}}\right), \tag{2.23}$$

where γ is an integration constant which is given in terms of the dimensionless surface charge $y = \frac{\lambda_B \sigma}{\kappa}$ by

$$\gamma = \frac{\sqrt{1+(y/2)^2}-1}{y/2} = \begin{cases} y/4, & |y| \ll 1; \\ 1, & |y| \gg 1. \end{cases} \tag{2.24}$$

From Eq. (2.23) we can find the surface potential on the plane by letting $z = 0$, this is formally known as the Gouy-Chapman Surface potential.
Applying (2.24) to (2.14) we obtain the ion density profiles for $z > 0$,

$$\rho_\pm(z) = \rho_b \left(\frac{1 \mp \gamma e^{-\kappa z}}{1 \pm \gamma e^{-\kappa z}}\right)^2. \tag{2.25}$$

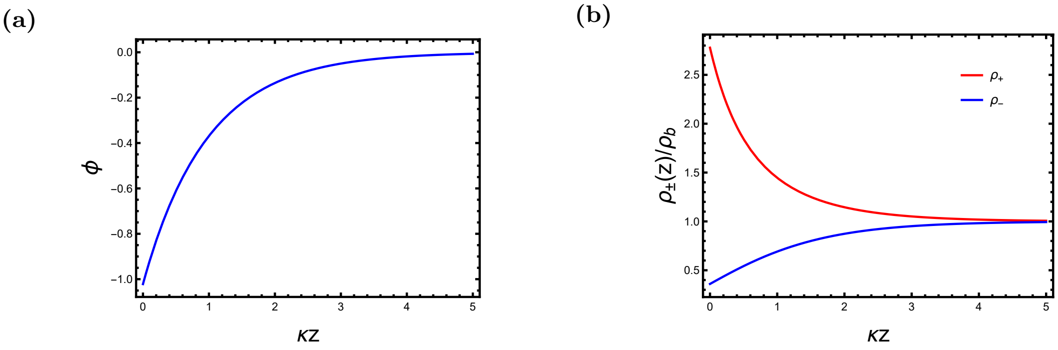

Figure 3: We evaluate the electric potential and the dimensionless salt concentration using (2.24) with the dimensionless value of $y = -1$. **(a)** We have the electric potential as described in a dimensionless plot using the equation (2.23). **(b)** We have the dimensionless salt concentration profiles where we used (2.25), and we divide the positive and negative salt concentrations with the bulk to make the equation dimensionless.

We evaluate equation (2.23) to produce a dimensionless electric potential as a function of the distance for a negatively charged surface potential $y = -1$, visualised in Figure 3(a). To describe the dimensionless salt concentration with respect to the dimensionless distance to the charged plane we use Eq. (2.25) and is visualised in Figure 3(b). We note that there is an induced negative electrostatic potential to the plane, this negative surface potential accumulates positive ions within the system and comparatively reduces the number of negative ions. However, within several dimensionless distance steps the electric potential no longer influences the liquid electrolyte. This can be seen in Figure 3(b) as the salt concentrations become equivalent to the bulk. Therefore, the information we can gather from Figures 3(a) and 3(b) is that the salt concentrations and electrostatic potentials are most concentrated close to the charged plane. This provides us with some intuition as to the nature of the Debye length, and the thickness of the electric double layer.

Since we will primarily be investigating the nature of cylindrical ionic channels, a natural progression is to move away from two planes in parallel to that of a cylinder. Assume an infinitely long cylindrical channel of radius R where the radius is substantially larger than that of the Debye length, $R \gg \lambda_D$. In doing so we can significantly simplify the equation for the electric potential by introducing the coordinate $r = R - s$ and write the Poisson equation for $s \ll R$ as

$$\nabla^2\phi(s) = \frac{1}{r}\frac{\partial}{\partial r}\left(r\frac{\partial\phi(s)}{\partial r}\right) = \frac{1}{R-s}\frac{\partial}{\partial(R-s)}\left((R-s)\frac{\partial\phi(s)}{\partial(R-s)}\right) \approx \frac{\partial^2\phi(s)}{\partial s^2}. \tag{2.26}$$

Therefore, we arrive back at a similar equation to the singular charged plane, where the Poisson-Boltzmann equation equates to

$$\frac{\partial^2\phi(s)}{\partial s^2} = \kappa^2\sinh(\phi(s)), \tag{2.27}$$

solving this equation we obtain the electric potential and the salt concentration distribution:

$$\phi(s) = 2\ln\left(\frac{1+\gamma e^{-\kappa s}}{1-\gamma e^{-\kappa s}}\right) = 2\ln\left(\frac{1+\gamma e^{-\kappa(R-r)}}{1-\gamma e^{-\kappa(R-r)}}\right), \tag{2.28}$$

$$\rho_\pm(s) = \rho_b\left(\frac{1\mp\gamma e^{-\kappa s}}{1\pm\gamma e^{-\kappa s}}\right)^2 = \rho_b\left(\frac{1\mp\gamma e^{-\kappa(R-r)}}{1\pm\gamma e^{-\kappa(R-r)}}\right)^2, \tag{2.29}$$

respectively. Interestingly, despite moving from a single plane to a cylindrical channel, we can note that γ is the same constant as described in Eq.(2.24).

2.4 Poisson-Nernst-Planck-Stokes (PNPS) Equation for Ionic Channels

We now analyse the transport of ions in a microfluidic system with fluid velocity $\mathbf{u}(x,r,t)$ and electric potential $\Psi(x,r,t)$ with x denoting the position along the length of the channel, $r \in [0,R]$ the radial component, and lastly t the time component, with the system in question having a dielectric constant ε. The system is assumed to have a positive homogeneous surface charge density $e\sigma = 0.1e$ nm^{-2}, which is constant along the length of the channel L. As in previous discussions in explaining an electric double layer, we will be dealing with a 1:1 liquid electrolyte, which has positive and negative ions of concentration ρ_+ and ρ_-, respectively.

Firstly in macro-dynamics, the Navier-Stokes equation for an incompressible fluid,

$$\rho_m\frac{\partial\mathbf{u}}{\partial t} + \rho_m(\mathbf{u}\cdot\nabla)\mathbf{u} = -\nabla p + \eta\nabla^2\mathbf{u} + \mathbf{f}, \tag{2.30}$$

$$\nabla\cdot\mathbf{u} = 0, \tag{2.31}$$

where $p(x,r,t)$ denotes the pressure profile, ρ_e is the ionic space charge density $\rho_e = \rho_+ - \rho_-$, and $\mathbf{f}$ an additional body force, as our system is concerned with electrostatic forces we have $\mathbf{f} = -\,e\rho_e\nabla\Psi$, this is the product the local charge density and electric field. There is no externally applied pressure to this system thus, $\nabla p = 0$. This is a rather complicated equation to work with due to its nonlinearity in velocity $\mathbf{u}$. However, in our case, as we are investigating a micro-fluidic system the velocity is small due to strong viscous forces, the Reynolds number $\mathrm{Re} = \frac{\rho_m ul}{\eta} \ll 1$. This equation represents the ratio of "inertia" and "viscous damping", where l, u, η, and ρ_m is the length scale, velocity, viscosity, and fluid mass density of interest, respectively. When we deal with an aqueous micro-fluidic channel [5] it causes $\mathrm{Re} \ll 1$ and allows us to remove the inertial term and provided that we are only in a steady state we reduce Eq. (2.13) to

$$\eta\nabla^2\mathbf{u} - e\rho_e\nabla\Psi = 0. \tag{2.32}$$

Note the two mechanical forces acting upon the system are that of a pressure gradient and the Coulomb force. We link the Navier-Stokes equation to the Poisson equation by observing that the ionic space charge density directly influences the electric potential,

$$\nabla^2\Psi = -\frac{e}{\varepsilon}\rho_e. \tag{2.33}$$

We impose the following boundary conditions for the Poisson equation $\Psi(-\infty, r, t) = V(t)$ and $\Psi(\infty, r, t) = 0$, meaning that on one side of the channel at an "infinite" distance we apply an electric potential and on the other, it is grounded respectively. To link the Navier-Stokes equation to the Poisson equation simply substitute the ionic space charge density ρ_e found in (2.33) into (2.32). Furthermore, expanding the equations required to fulfil the desired iontronic channel, we begin by noting that the ionic fluxes $\mathbf{j}_\pm$ and the concentration profiles $\rho_\pm$ must satisfy the continuity equation

$$\frac{\partial \rho_\pm}{\partial t} + \nabla \cdot \mathbf{j}_\pm = 0, \tag{2.34}$$

along with the Nernst-Planck equation

$$\mathbf{j}_\pm = -D_\pm \left(\nabla \rho_\pm \pm \rho_\pm \frac{e \nabla \Psi}{k_B T} \right) + \mathbf{u} \rho_\pm. \tag{2.35}$$

The three terms in (2.35) correspond to Fickian diffusion, Ohmic conduction, and Stokesian convection, respectively. Combining Eqs. (2.31)-(2.35) we obtain the Poisson-Nernst-Planck-Stokes (PNPS) equations which allow us to study the transport of ions through the channel. Furthering the boundary conditions for this model we assume the no-slip condition $\mathbf{u}(x, r = R, t) = 0$ on a solid wall, here we let R denote the distance to the wall from the centre of the channel, the blocking condition $\mathbf{n} \cdot \mathbf{j}_\pm = 0$, and Gauss' law $\mathbf{n} \cdot \nabla \Psi(x, R, t) = e\sigma(x)/\varepsilon$.

2.5 Transport Equations

Building upon the set of PNPS equations we now look toward how ions are transported through a channel. We will use a perfectly symmetric cylindrical channel with a homogeneous surface charge connecting two reservoirs as seen in Figure 4, this channel is of length L and radius R containing a liquid 1:1 electrolyte at room temperature. We will take inspiration from Ref. [46] where Werkhoven et al. delve into local linear response theory to describe the transport of ions. There are three driving forces which may be imposed onto any channel, pressure $\partial_x p$, voltage $\partial_x V$ and chemical potential $\partial_x \mu$ drop. These driving forces induce three fluxes in return, volume fluid flow Q, electric current I, and salt flux J. It was found using linear response theory that it is possible to relate the driving forces with the fluxes. The well-known method of combining

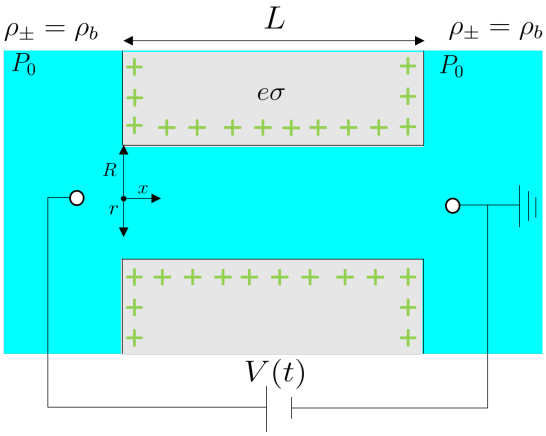

Figure 4: Schematic representation of an axially symmetric homogeneous unipolar channel, with channel length L, radius R. The channel connects two bulk reservoirs of 1:1 electrolytes with bulk concentration ρ_b. Along the channel surface, we apply a uniform surface charge density $e\sigma$. An electric potential, $V(t)$, is applied to the bulk reservoir at an infinite distance from the channel on the left-hand side and then grounded in the opposite reservoir. The channel does not have an externally applied pressure denoted by P_0 in each reservoir.

these transport equations is by using the Onsager matrix L [32, 33] and is of the form

$$\begin{pmatrix} Q \\ I \\ J - 2\rho_s Q \end{pmatrix} = A\mathbf{L} \begin{pmatrix} -\partial_x p \\ -\partial_x V \\ -\partial_x \mu \end{pmatrix}, \tag{2.36}$$

where $\mathbf{L}$ is a 3×3 symmetric matrix, A is the cross-sectional area of the channel. We note that for the chemical potential driving force, the related flux is that of the excess salt flux, the reason why this distinction must be made is to ensure that the Onsager matrix is symmetric. We can impose numerous boundary conditions on this system to create well-known transport phenomena such as electro-osmosis where there is only an electric potential drop across the channel, streaming potential where the system just experiences a pressure drop, and lastly, diffusio-osmosis where only the chemical potential drop is the sole driving force within the system [46]. The way in which we solve the Onsager matrix is by using the previously mentioned boundary conditions as well as a number of others and equating certain elements to their respective fluxes.

Let's now discuss the fluxes in Eq. (2.36), these fluxes originate from two sources

$$Q = 2\pi \int_0^R r u_x(r)\,\mathrm{d}r, \tag{2.37}$$

$$I = 2\pi e \int_0^R r(j_{+,x}(x,r) - j_{-,x}(x,r))\,\mathrm{d}r, \tag{2.38}$$

$$J = 2\pi \int_0^R r(j_{+,x}(x,r) + j_{-,x}(x,r))\,\mathrm{d}r. \tag{2.39}$$

The volume flow through the channel is the cross-sectional average velocity through the channel. To derive such a fluid flow we solve for the velocity using the Navier-Stokes equation (2.32) with the relevant system boundary conditions. The electric current and the total salt flux depend upon the Nernst-Planck equation (2.35) where there's a reliance on the diffusive nature of the system along with the momentum of fluid. We can obtain the total salt flux by summing the ion fluxes $j_\pm(x,r)$ and also by noting that the electric current travels via the transport of ions within the channel. Therefore, to get the average electric current we must compute the difference between the flux of the positive and negative ions, if the majority flux is negative we have a negative current flowing through the channel for example.

3 An Investigation of Flow in a Cylindrical Ionic Channel

3.1 Unifying the Theory

In Section 2, we introduced the theory surrounding ionic channels with an applied homogeneous surface charge density. In this section, we analyse the transport of ions through a cylindrical channel with an inhomogeneous surface charge density. In literature there have been discussions suggesting that the set of PNPS equations with the transport equations can describe the nature of such channels [3, 18, 19, 46]. In simple cases, the mechanisms driving the cylindrical channel with a homogeneous surface potential are well known, however in breaking the symmetry of the channel by applying an inhomogeneous surface charge density the robust understanding of the system no longer exists. Therefore, we will provide a unified theory for cylindrical bipolar channels.

3.2 The Physics of Cylindrical Bipolar Channels

The cylindrical channel of interest is represented by the detailed schematic in Fig. 5(a). We apply an electric potential drop across the channel described by Figure 5(b) where we apply a static voltage of $V = 1$ V infinitely far from the channel located at $x = -\infty$ nm and grounded at $x = \infty$ nm. In Figure 5(b) the channel resides within the dotted red lines. We consider two bulk reservoirs containing a liquid 1:1 electrolyte with a mass density $\rho_m = 10^3\ \mathrm{kg \cdot m^{-3}}$, viscosity $\eta = 1.01\ \mathrm{mPa \cdot s}$, electric permittivity $\varepsilon = 0.71\ \mathrm{nF \cdot m^{-1}}$, the ions have diffusion coefficients $D_\pm = D = 2\ \mu\mathrm{m}^2 \cdot \mathrm{ms}^{-1}$ [26]. The two reservoirs are connected by a cylindrical channel of radius $R = 200$ nm. The base of the channel is the point at which $x = 0$ and the

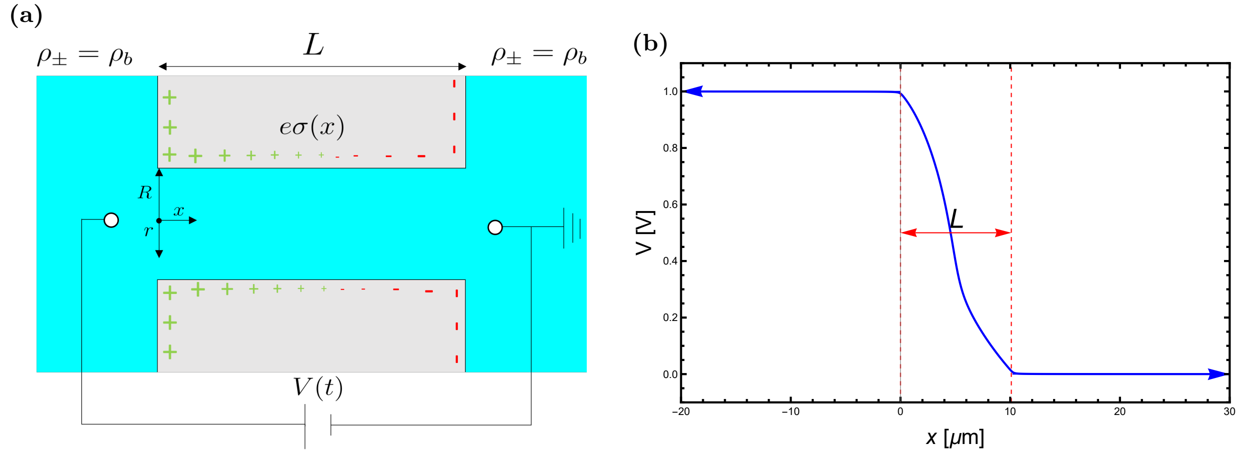

Figure 5: **(a)** Schematic representation of an axially symmetric cylindrical bipolar channel, with channel length L, radius R. The channel connects two bulk reservoirs of 1:1 electrolytes with bulk concentration ρ_b. Along the channel surface, there is a homogeneous surface charge density $e\sigma(x)$, represented by Eq. (3.1). An electric potential, $V(t)$ is applied to the bulk reservoir at an infinite distance from the channel on the left-hand side and then grounded in the opposite reservoir. **(b)** Finite element calculation of the electric potential drop across the cylindrical channel. The channel is residing within the red dotted lines with an applied voltage of $V = 1$ V.

tip $x = L = 10$ μm, where x denotes the position along the channel and r is the radial component of the system with the central axis positioned at $r = 0$. We assume an inhomogeneous surface charge density $e\sigma(x)$ positioned along the walls of the channel, $r = R$. The surface charge density linearly increases along the length of the channel and is described as

$$\sigma(x) = \sigma_0 + \sigma' \frac{x}{L} = \sigma_0 \left(1 + \frac{\sigma'}{\sigma_0} \frac{x}{L}\right), \tag{3.1}$$

where $e\sigma_0 = 0.1e$ nm^{-2} at the base of the channel and $e\sigma'$ induces the inhomogeneity. The value of σ' will vary through the course of this thesis, thus we will define it when required. For simplicity, we will create a reference surface charge density that we will use throughout this thesis and is $e\sigma_{ref} = 0.1e$ nm^{-2}, this will allow us to vary the surface charge density with respect to the reference. For example, there is a channel wherein the surface charge density is positive at the base and negative at the tip. To do so $\sigma' < -\sigma_0$ such that the surface charge changes sign between $x = 0$ and $x = L$. We impose fixed ion concentrations on both reservoirs, which are at an infinite distance from the channels, $\rho_\pm = \rho_b = 2$ mol $\cdot$ m^{-3}. Therefore, the surface potential ψ_0 known also as the zeta potential can be described by the equilibrium Gouy-Chapman surface potential Eq. (2.28) by setting $s = 0$,

$$\psi(x) = \frac{2k_BT}{e} \sinh^{-1}(2\pi\lambda_B\lambda_D\sigma(x)). \tag{eq:3.2}$$

We assume the system is at room temperature, therefore $k_BT = 4.11 \cdot 10^{-21}$ J with an approximate constant Debye length of $\lambda_D \approx 6.8$ nm. We impose the same boundary conditions as seen in Section 2.3. As detailed in Fig 5(a), we assume that the only driving force acting on this system is that of an electric potential drop. At an infinite distance from the channel, we apply a voltage and at an infinite distance in the opposite opposite reservoir the system is grounded, we are then left with a potential drop of $\Delta V = V$. Our system is similar to the systems in Ref. [18] with the primary difference originating from the geometry of the system.

3.3 The Theoretical Model for Cylindrical Channels

In this section, we investigate how flow affects the nature of an ionic channel. In doing so, we will create a consistent set of equations that do not require parametric fits to describe the volumetric flow of a fluid through a cylindrical channel. The derivations we will use for this section largely originate from Refs. [3, 18].

To begin we derive an expression for the total flux $J(x)$ Eq. (2.39); to do so we must make several assumptions. We assume that the channel radius is much smaller than the length of the channel; this is commonly known as the long-channel limit. The purpose of this assumption is to reduce the entrance effects such that they can be disregarded. The entrance effects can produce a radial flux component but if we impose a long channel the lateral flux dominates such that we can ignore the radial component. Another method we use to simplify the complex PNPS equations is to impose that the radius of the channel is much smaller than the Debye length. These two approximations allow us to assume that the salt concentration is approximately equal to the radially average salt concentration $\rho_s(x,r) \approx \bar{\rho}_s(x)$ and the electric field is radially independent $\partial_x \Psi(x,r) \approx \partial_x \Psi(x)$ this gives us the slab average electric field for only a small number λ_D away from the surface of the channel. We will now compute the total salt flux using (2.39),

$$\begin{aligned} J(x) &= 2\pi \int_0^R \left(-D\left(\nabla\rho_+(x,r) + \rho_+(x,r)\frac{e\nabla\Psi}{k_B T} \right) + \mathbf{u}\rho_+(x,r) - D\left(\nabla\rho_-(x,r) - \rho_-(x,r)\frac{e\nabla\Psi}{k_B T} \right) + \mathbf{u}\rho_-(x,r) \right) r\,\mathrm{d}r, \\ &\approx -2\pi D \int_0^R \left(\partial_x\bar{\rho}_s(x) + \bar{\rho}_e(x)\frac{e\nabla\Psi}{k_B T} \right) r\,\mathrm{d}r + Q(V)\bar{\rho}_s(x). \end{aligned} \tag{3.3}$$

Here we used that volumetric flow is defined in Eq. (2.37). We note that the charge density ρ_e is negligible outside of the Debye length of the EDL, using this we can deduce that the space charge density contributes only from the EDL. We then use Gauss' law in combination with the Poisson equation (2.33) to introduce the surface charge into the total salt concentration

$$\begin{aligned} \int_0^R r\nabla^2\Psi(x,R)\,\mathrm{d}r &= \int_0^R r\frac{e}{\varepsilon}\rho_e\,\mathrm{d}r, \\ \therefore \int_0^R r\rho_e\,\mathrm{d}r &= -e\sigma(x). \end{aligned} \tag{3.4}$$

We now wish to simplify the total salt flux expression by solving the electric field $\nabla\Psi$. To begin we compute the radially averaged electric potential

$$\bar{\Psi}(x) = 2\pi \int_0^R \frac{\Psi(x,r)}{\pi R^2} r\,\mathrm{d}r. \tag{3.5}$$

Neglecting external space charges outside of the electric double layer we can determine the electric field. We assume that the only charge acting upon the system originates from the electric double layer, therefore, we note that the rest of the system is assumed to be neutral. This means that the electric field must be divergence-free. Using this assumption the average electric field must be proportional to the inverse cross section to be divergence-free i.e. $\partial_x\bar{\Psi}(x) = \frac{C}{\pi R^2}$, where C is a constant. A proportionality constant follows from the condition that

$$\int_0^L \partial_x\bar{\Psi}(x)\,\mathrm{d}x = -V. \tag{3.6}$$

Applying the proportionality condition we solve for the constant C,

$$\begin{aligned} \int_0^L \partial_x\bar{\Psi}(x)\,\mathrm{d}x &= \int_0^L \frac{C}{\pi R^2}\,\mathrm{d}x, \\ &= \frac{CL}{\pi R^2}, = -V. \end{aligned} \tag{3.7}$$

Integrating (3.5) we find the constant in question to be $C = -\frac{\pi R^2 V}{L}$, therefore, accumulating these expressions and conditions we arrive at the cross-sectional electric field

$$\partial_x \bar{\Psi}(x) = -\frac{V}{L}. \tag{3.8}$$

We now implement these expressions into the total salt concentration (3.3) and integrate the radial component to obtain

$$J(x) = -D\left(\pi R^2 \partial_x \bar{\rho}_s(x) + 2\pi\sigma(x)\frac{eV}{k_B T}\frac{R}{L}\right) + Q(V)\bar{\rho}_s(x), \tag{3.9}$$

the total salt flux through a cylindrical channel.

The final unknown expression in the total salt flux equation is the volumetric flow $Q(V)$. To begin we must solve the Navier-Stokes equation for an electro-osmotic system. The fluid only has a lateral velocity through the channel and due to the fluid being incompressible the velocity only depends on the radial component, $\mathbf{u}(\mathbf{r}) = (u_x(r), 0, 0)$. Therefore, we assume no turbulence occurs within the channel and Eq. (2.32) becomes

$$\eta\nabla^2 u_x(r) + \rho_e E_x = 0, \tag{3.10}$$

where $E_x = V/L$ is the difference in the electric potential over the length of the channel. Using the Poisson equation (2.33) we have a closed-form equation which can be solved for the velocity if we impose the no-slip condition $u_x(R) = 0$ we obtain

$$u_x(r) = \frac{\varepsilon V}{L}(\Psi(r) - \Psi_0), \tag{3.11}$$

where Ψ_0 is a constant of integration. We can now implement the velocity into the volume flow equation from (2.37).

$$\begin{aligned} Q &= 2\pi\frac{\varepsilon V}{L}\int_0^R r(\Psi(r) - \Psi_0)\,\mathrm{d}r, \\ &= -\pi R^2\frac{\varepsilon V \Psi_0}{\eta L} + 2\pi R\frac{\varepsilon V}{\eta L}\int_0^R r\Psi(r)\,\mathrm{d}r. \end{aligned} \tag{3.12}$$

We refer to Ref. [46] to note that the second term can be neglected as we can substitute a Boltzmann expression which introduces the Debye length. Due to the Debye length being involved in the second term, we can use our assumption that $R \gg \lambda_D$ [2] and approximate the volume fluid flow to be

$$Q(V) = -\pi R^2\frac{\varepsilon V \Psi_0}{\eta L}. \tag{3.13}$$

As the potential Ψ_0 resides on the surface of the channel, we assume that this potential is the surface potential across the channel thus we change the notation to $\Psi_0 = \bar{\psi}$ [3, 46]. This constant must be laterally averaged across the channel because the fluid is incompressible hence the volumetric flow is the same across all points in the channel. Now that we have introduced all of the prerequisite equations, we can solve for the radially averaged salt concentration profile $\bar{\rho}_s(x)$. Note the total salt flux must be divergence-free within the steady-state regime, $\partial_x J = 0$. Using this condition along with imposing boundary condition $\rho_s(0) = \rho_s(L) = 2\rho_b$ yields the radially averaged salt concentration for a bipolar cylindrical channel given by

$$\bar{\rho}_s(x, V) = 2\rho_b - \frac{1}{\mathrm{Pe}/V}\frac{2e\sigma'}{k_B T R}\left(1 - \frac{x}{L} - \frac{e^{-\mathrm{Pe}(1-x/L)} - 1}{e^{-\mathrm{Pe}} - 1}\right). \tag{3.14}$$

We introduced in Eq. 3.14 the dimensionless Péclet number, $\mathrm{Pe} = Q(V)L/(\pi D R^2)$. The Péclet number is defined as the product of the Reynolds number Re, defined in Section 2.4, and the Schmidt number Sc which is the ratio of mass and momentum diffusivity. In essence, this creates an expression which incorporates the fluid flow and the diffusivity of the system [34]. We now evaluate the radially averaged salt flux to gain a physical interpretation of the nature of Eq. (3.14). We set the inhomogeneous part of the surface charge $\sigma'/\sigma_0 = -3/2$ to create a bipolar cylindrical channel.
The last parameter which needs to be evaluated is the laterally averaged

$$\bar{\psi} = \frac{1}{L}\int_0^L \frac{2k_BT}{e}\sinh^{-1}(2\pi\lambda_B\lambda_D\sigma(x))\,\mathrm{d}x, \tag{3.15}$$

which evaluates to $\bar{\psi} \approx 26$ mV [3, 18]. Now the radially averaged salt concentration can be computed.

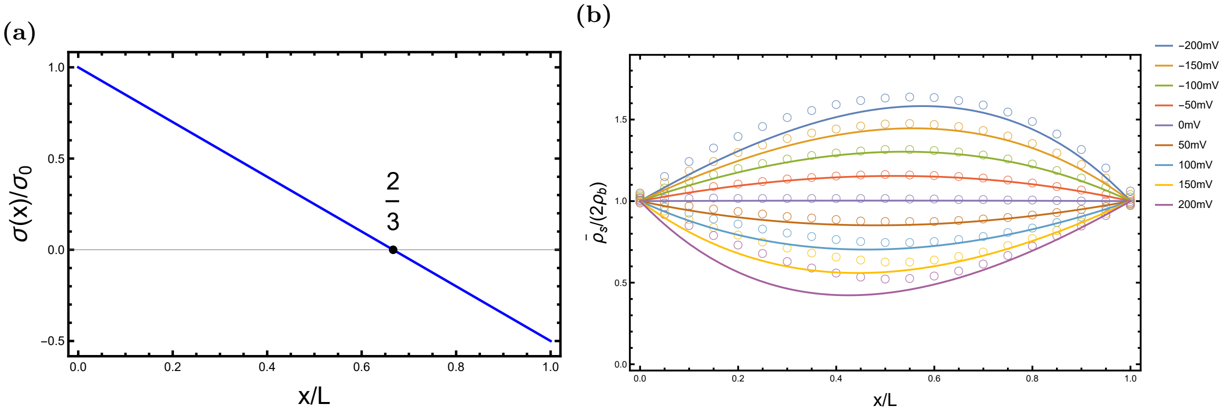

Figure 6: **(a)** Dimensionless surface charge density of a bipolar channel as a function of x/L, the length of the channel described by Eq. (3.1). We set $\sigma'/\sigma_0 = -3/2$ which provides us with a zero-point located at $(2/3, 0)$. Here the surface charge density is $e\sigma_0 = e\sigma_{ref} = 0.1e\ \mathrm{nm}^{-2}$. **(b)** Comparison between finite-element (FE) calculation represented by circles and the radially averaged salt concentration profiles calculated by an analytical approximation (AA) denoted by solid lines for a bipolar cylindrical channel. We take various electric potentials $V \in [-200, 200]$ mV indicated by the colours next to the diagram.

In Figure 6(a) we plotted the dimensionless surface charge density as a function of the length of the channel. We note that the surface charge density is zero at the ratio between the initial and final surface charge density values i.e. σ_0/σ' is the location at which $\sigma(x) = 0$. In Figure 6(b), we compare the analytical approximation (AA) evaluated using Eq. (3.14) with the finite-element (FE) calculations obtained through the use of COMSOL. The range of electric potentials applied to the system is $V \in [-200, 200]$ mV. Studying Figure 6(b), we learn that we have an accumulation of ions approximately biased towards two-thirds of the way through the cylinder for negative electric potentials. In contrast, for positive potentials, there is a depletion of ions with a bias towards the base. The FE and AA solutions have a good relationship with each other except for the positive electric potentials where there is a growing difference emerging seen with the $V = 200$ mV. We note that in the calculation of Figure 6(b) we implemented an ad-hoc method to ensure that the radially averaged salt concentration does not become negative. If our AA solution reduces past 10% of the bulk concentration we neglect the result and set the concentration to $\bar{\rho}(x, V) = 0.2\rho_b$, while not observed in the Figure 6(b) it is worth noting for future sections.

3.4 Analysis of Volumetric Flow

In this section, we aim to gain a greater understanding of the nature of the volumetric flow. This will allow us to definitively state that we have a set of equations that is self-contained meaning we do not require the use of a fit parameter for each change in surface charge density. To begin we use the same system parameters to create Figure 6(b), where $\sigma'/\sigma_0 = -3/2$.

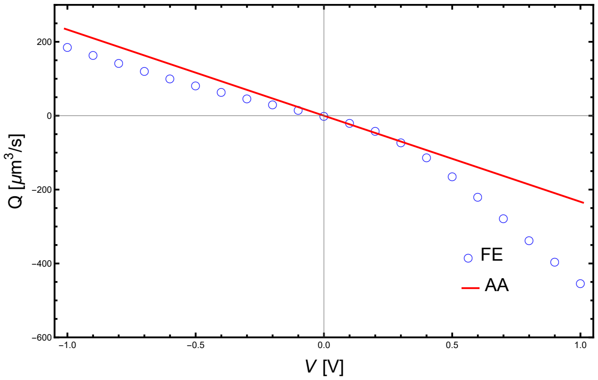

Figure 7: Volumetric flow as a function of the applied static electric potential V for a bipolar cylindrical channel with electric charge density $\sigma(x) = \sigma_0\left(1 + 3/2\frac{x}{L}\right)$ with $e\sigma_0 = 0.1e$ nm^{-2}. Comparing the FE calculations denoted by empty circles with the laterally averaged Gouy-Chapman surface potential which equates to $\bar{\psi} = 26$ mV.

In Figure 7, we plot the volumetric flow as a function of applied electric potential within the steady-state regime. The surface charge density is described as $\sigma(x) = \sigma_0\left(1 + 3/2\frac{x}{L}\right)$ with $e\sigma_0 = e\sigma_{ref}$. We see that there is a non-linearity presenting within the volumetric fluid flow only occurring in the positive electric potential regime as seen in the bottom right quadrant of Figure 7. While this is an interesting occurrence we still note that the linear equation Eq. (3.13) for volume flow has a reasonable agreement until reaching positive voltages. However, this is only for one surface charge density, we must test if $Q(V)$ captures the nature of the volumetric flow for varying surface charge densities.

Before we delve into answering this question, we want to reformulate Eq. (3.1), the surface charge density, to give a more physical meaning behind the equation. If we have a bipolar channel there will always be a so-called zero-point for the surface charge along the channel where $e\sigma(x) = 0$. This position we will denote by x_0. Therefore, we revise (3.1) to become

$$\sigma(x) = \sigma_0\left(1 - \frac{x}{x_0}\right), \tag{3.16}$$

where $x_0 = -\frac{L\sigma_0}{\sigma'}$, if $x_0 \in [0, L]$ we say that we have a bipolar channel. The initial surface charge density σ_0 we will refer to as the governing surface charge which we will use in combination with σ' to vary the zero-points. This simplifies the equation such that we are only required to supply the initial surface charge density and where we would like the zero point to be located. Using this restructured equation for the surface charge density we vary x_0 to test that the linear volume flow remains consistent for various surface potentials.

By evaluating the volumetric flow for $x_0 \in [0.3L, 0.7L]$ we obtain Figure 8(b), where the volumetric flow is computed as a function of the electric potential V. The first notable result is for $x_0 = 0.5L$, this illustrates that we have a perfectly anti-symmetric surface charge density and in creating such a system the flow is reduced to zero and is perfectly captured by Eq. (3.13) using the laterally averaged Gouy-Chapman surface potential Eq. (3.15). Creating an asymmetric surface charge density by setting x_0 to the remaining values listed we obtain a flow through the channel. To further enlighten our understanding of this asymmetry we can refer to Appendix A to view the velocity streamlines present in COMSOL computations. The linearity for negative electric potentials remains to be a reasonable agreement to FE results with the notable exception of $x_0 = 0.3L$. The reason for this discrepancy could arise due to the surface potential ranging from $\psi \in [93, -136]$ mV, the range denotes the base and tip surface potential respectively, comparing this to $x_0 = 0.7L$ which has a range of $\psi \in [93, -55]$ mV we note that this range does not vary to the same extent indicating a possible range where our theory is optimal.

While the volumetric flow is with one exception captured reasonably well for negative electric potentials, the non-linearity present in the positive regime needs to be addressed. To capture this deviation for a linear flow we look to Eq. 3.13. We assume that all elements in this equation do not vary with electric potentials. However, the laterally averaged surface potential Eq. (3.15) has one component which may induce non-linearity, that of the Debye length. We have assumed that the Debye length is constant Eq. (2.11) but referring to Ref. [45] Chapter 8 we find that the Debye length varies with the salt concentration.

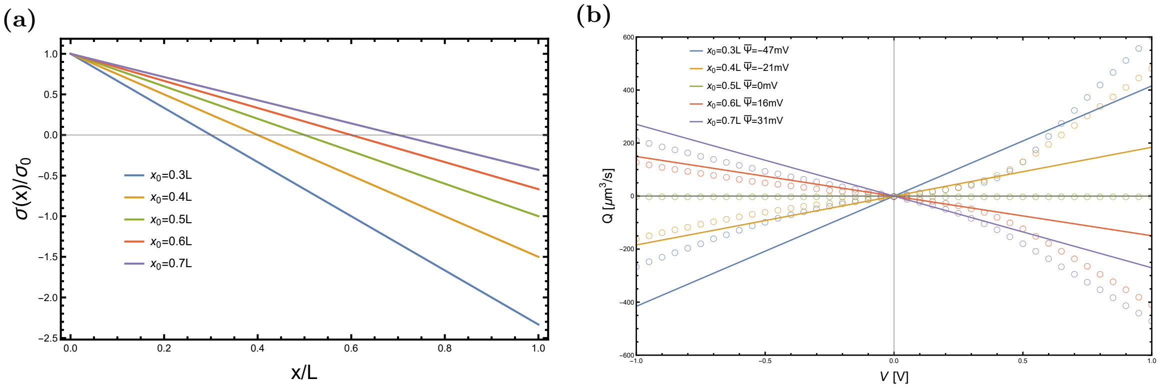

Figure 8: **(a)** The surface charge density along the length of the channel for various zero points in the range $x_0 \in [0.3L, 0.7L]$.**(b)** Volumetric flow as a function of applied static electric potential for bipolar channels with varying surface charge densities. The governing surface charge density is $e\sigma_0 = 0.1e\,\mathrm{nm}^{-2}$ with the zero point calculated using (3.16) such that we have $x_0 \in [0.3L, 0.7L]$ with corresponding laterally averaged surface potentials of the range $\bar{\psi} \in [-47, 31]$ mV as indicated by the colours. Comparing finite element calculations with analytical approximations for the volumetric flow represented by empty circles and solid lines, respectively.

Therefore, noting from Figure 6(b) where we depict the salt concentration as a function of channel length, the salt concentrations vary with electric potential. We can incorporate the radially average salt concentration profile into the Debye length with the following equation

$$\lambda_D(x, V) = \left(\frac{\varepsilon k_B T}{2\rho_b e^2}\right)^{1/2} \left(\frac{2\rho_b}{\bar{\rho}_s(x, V)}\right)^{1/2}. \tag{3.17}$$

Note that similarly to the radially averaged salt concentration profile seen in Figure 6(b) we have implemented an ad-hoc cut-off point so that our AA solution does not incorporate negative salt concentrations which are not physical. We can now input this into the laterally averaged Gouy-Chapman surface potential

$$\bar{\psi}(V) = \frac{1}{L}\int_0^L \frac{2k_B T}{e}\sinh^{-1}(2\pi\lambda_B\lambda_D(x, V)\sigma(x))\,\mathrm{d}x, \tag{3.18}$$

to provide us with the desired non-linearity in the electric potential V. This non-linear zeta potential causes a self-consistency issue. In order to implement the radially averaged salt concentration equation we require the volumetric flow within the equation. Thus, we have in essence created a loop within our equations. To mitigate the self-consistency issue, we propose an iterative method where one starts with the linear volumetric flow described by (3.15) and (3.13) and call this Q_0. Using this initial volumetric flow Q_0 we substitute it into the Péclet number found in Eq. (3.14) to create the non-linear Debye length. Once we have formulated the non-linear Debye length we then compute

$$\bar{\psi}(V, Q_0) = \frac{1}{L}\int_0^L \frac{2k_B T}{e}\sinh^{-1}(2\pi\lambda_B\lambda_D(x, V, Q_0)\sigma(x))\,\mathrm{d}x, \tag{3.19}$$

to give us the first iteration of the non-linear flow

$$Q_1(V) = -\pi R^2\frac{\varepsilon V\bar{\psi}(V, Q_0)}{\eta L}. \tag{3.20}$$

A pictorial diagram aids in the understanding of this iterative method seen in Figure 9(a). The loop begins with the linear volume flow denoted by Q_0 and then is substituted into the radially averaged salt concentration to provide a Debye length that is dependent on x and V. We take the laterally averaged Gouy-Chapman surface potential which creates the first iteration. After several iterations i we eventually arrive at the final iteration denoted by the subscript n.

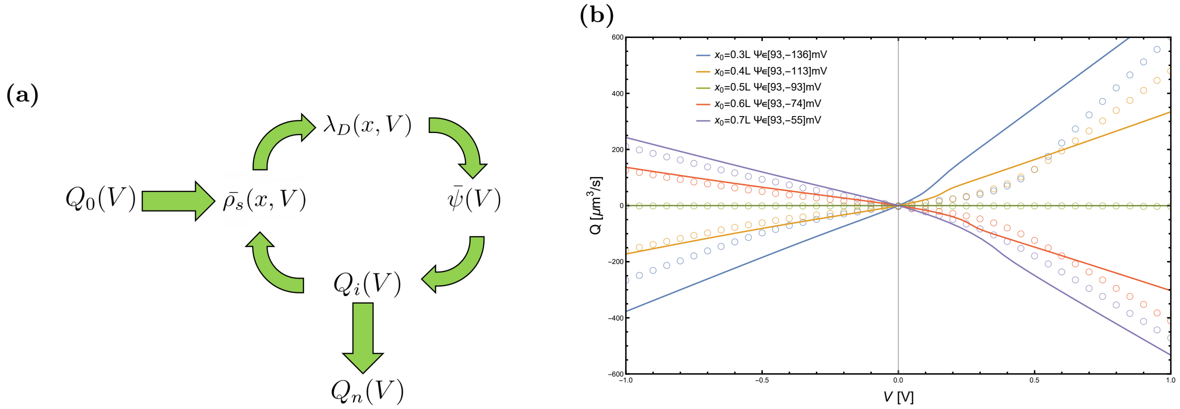

Figure 9: **(a)** Diagram displaying the iterative method used to create a non-linear flow for a cylindrical channel. The subindices i and n denote the iteration within the loop and the final output iteration, respectively. **(b)** Comparison between FE calculation represented by circles and the volumetric flow in the solid line. We vary the zero-point x_0 between $0.3L$ and $0.7L$ with $e\sigma_0 = e\sigma_{ref}$. We implement our first iteration of the non-linear volumetric flow, Q_1.

In Figure 9(b), we only introduced the first iteration for the non-linear volume flow as a function of voltage V within the steady-state regime. The bipolar channels have governing surface charge density $e\sigma_0 = e\sigma_{ref}$. We note that the negative regime does have some minor improvement if we compare it to Figure 8(b), a diagram of linear volumetric flow. The positive electric potentials have significant improvements in capturing the flow by implementing the radially averaged salt concentration into the Debye length. There is a notable improvement over the linear theory especially for $x_0 = 0.7L$ and $x_0 = 0.6L$ where the analytical result is within good agreement with the FE calculation. This may mean that there is a range within which our theory provides optimal results, and outside of which generates less optimal results. However, this is our first iteration and we note that there are two questions which arise from this method; how many iterations n as seen in our diagrammatic Figure 9(a) of the iterative process does it take to converge to a specific non-linear curve, and what is the optimal surface potential range?

Regarding the first question, unfortunately, there is not a clear answer to this. With some volume flows specifically $x_0 = 0.3L$, it converges to within two iterations and with others for example $x = 0.7L$ it may take up to eight iterations until the result has converged to a consistent result. We maintain the governing surface charge density at $e\sigma_0 = 0.1e$ nm^2 for each of the different zero points. Therefore, to achieve $x_0 = 0.3L$ we require a proportionally larger σ'. Due to the larger σ' the Debye length reaches its maximal value of $\lambda_D = 22$ nm as a result of the implementation of the ad-hoc method for the radially average salt concentration. This ensures there are no negative salt concentrations present in our analytical solution.

In Figure 10 where the volumetric flow is a function of the electric potential with governing surface charge density $e\sigma_0 = e\sigma_{ref}$ with eight iterations applied. The non-linearity does not change for $x_0 = 0.3L$ and $x_0 = 0.4L$ for positive electric potentials. It arises from the gradient transition of the surface charge density from positive to negative being much larger than the other surface potentials. We note also that in the positive voltage regime, the volumetric flow becomes linear. This implies that we have reached the maximum Debye length of 22 nm allowed by our salt concentration with the ad-hoc minimal depletion, $\bar{\rho}(x, V) = 0.2\rho_b$. In Figure 10, $x_0 = 0.6L$ and $x_0 = 0.7L$ have improved their agreement with the finite element calculations. We can deduce from this that there is a range of surface potentials and our iterative method can produce a good agreement with numerical analysis.

Now we will look toward finding the optimal surface potential range that our equations can accurately model. We begin by reducing the governing surface charge density. Previously, we set $e\sigma_0 = 0.1e$ nm^{-2}, now we will reduce this to 20% and 50% of this value, we will denote this by letting $e\sigma_0 = 0.2e\sigma_{ref}$ and $e\sigma_0 = 0.5e\sigma_{ref}$, respectively.

We can still use the same equation for the zero-points Eq. (3.16), merely with the different values for the governing surface charge density, σ' will effectively be scaled to maintain the desired zero-points. In Figure 11(a) we plot the volumetric flow against the static electric potential V with the governing surface charge density reduced to $e\sigma_0 = 0.2e\sigma_{ref}$. This lowers the surface potentials across the channel to be within

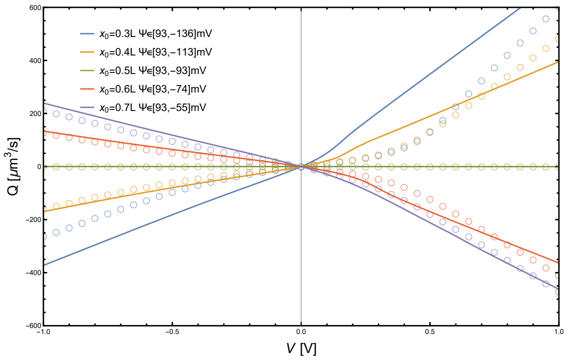

Figure 10: Volumetric flow plotted as a function of an applied static electric potential V with governing surface charge density of $e\sigma_0 = e\sigma_{ref}$. Using this surface charge density we vary the zero point between the range $x_0 \in [0.3L, 0.7L]$. The associated surface potentials are indicated in the diagram with the associated zero point, the range begins with the surface potential at $x = 0$ to $x = L$. Comparison between FE calculation represented by circles and the volumetric flow in the solid line. We implemented the fully converged non-linear volumetric flow by computing the eighth iteration, Q_8.

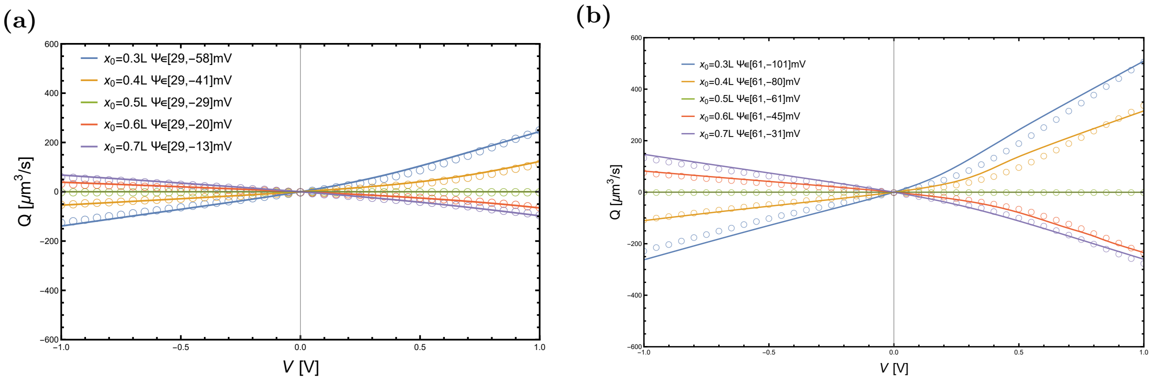

Figure 11: Plotting the volumetric flow as a function of the applied static electric potential for bipolar cylindrical channels. Comparing FE depicted as empty circles with volumetric flows represented by solid lines for different governing surface charges. We indicate the range of surface potentials associated with each zero point in the diagram, where the first value is the surface potential at $x = 0$ and the second $x = L$. The diagrams are of fully converged non-linear volumetric flow functions with eight iterations each. **(a)** This depicts the volumetric flow for a reduced governing surface potential to $e\sigma_0 = 0.2e\sigma_{ref}$ this reduction produces less non-linearity within the system except for $x_0 = 0.3L$. **(b)** Now we increased the governing surface charge density to $e\sigma_0 = e\sigma_{ref}$, producing more non-linearity but with our AA capturing with good agreement, especially with $x_0 = 0.3L$.

the range of approximately $\psi \in [29, -58]$ mV. The reduction allows for a greatly improved agreement with the numerical data with even the previously more extreme case $x_0 = 0.3L$ being captured by the iterative method. Figure 11(a) and 11(b) used eight iterations to create these non-linear diagrams.

Increasing the governing surface charge density to $e\sigma_0 = 0.5e\sigma_{ref}$ we have Figure 11(b), a volumetric flow diagram plotted against the steady-state voltage. If we increase the governing surface charge more than $e\sigma_0 > 0.5e\sigma_{ref}$ we return to a similar diagram as seen in Figure 10 where if $x_0 < 0.5L$ the numerical calculation no longer correlates with the analytical approximation. For $e\sigma_0 = 0.5e\sigma_{ref}$ we capture the volumetric flow with a high degree of accuracy for all values of x_0 which we consider to be the optimal regime. Experimental realisations of iontronic devices with a surface potential in the range of $\psi \in [61, -101]$ mV have been created Refs. [3, 16, 17]. Therefore, this model is physically possible to recreate within an experiment. As previously mentioned we investigated the number of iterations required to achieve a converged result.

In Figure 12 we plot multiple iterations of the analytical volumetric flow with the finite element calculation to correlate the result. We used the optimal initial surface charge density $e\sigma_0 = 0.5e\sigma_{ref}$ with the zero-point $x_0 = 0.7L$. This zero-point provides a converged volume flow that captures the finite element analysis perfectly. We began with the initial linear flow Q_0 and then proceeded with the iterative method described by Figure 9(a). While the negative electric potentials converged within a single iteration the positive regime requires eight iterations to achieve a complete convergence. For further sections, we will continue to use the fully converged volumetric flow of eight iterations.

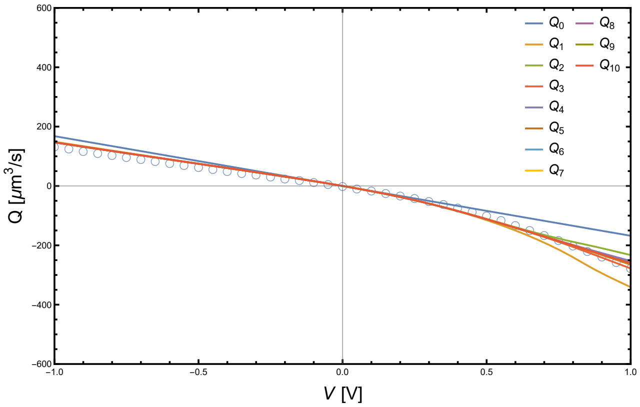

Figure 12: Iterative investigation of the volumetric flow as a function of the applied static electric potential. The zero-point used is $x_0 = 0.7L$ with the governing surface charge being $e\sigma_0 = 0.5e\sigma_{ref}$. The surface potential for this system is within the approximate range $\psi \in [61, -31]$ mV. The various iterations are represented by solid lines which we compare to the finite element calculation represented by empty circles. The surface potential ranges from $\psi \in [61, -31]$ mV, where the first value signifies the surface potential at $x = 0$ and the second at $x = L$.

3.5 The Effect of Varying the Zero-Point on the Salt Concentration Profiles

In this section, we will inspect the effect of changing the zero-point, x_0, on the salt concentration profile. The surface charge density zero-points we will discuss are that of $x_0 = 0.3L$, $x_0 = 0.5L$ and $x_0 = 0.7L$, where we have set the governing surface charge density to be $e\sigma_0 = 0.5e\sigma_{ref}$. This surface charge density has excellent agreement with our volume flow equation as seen in Figure 11(b).

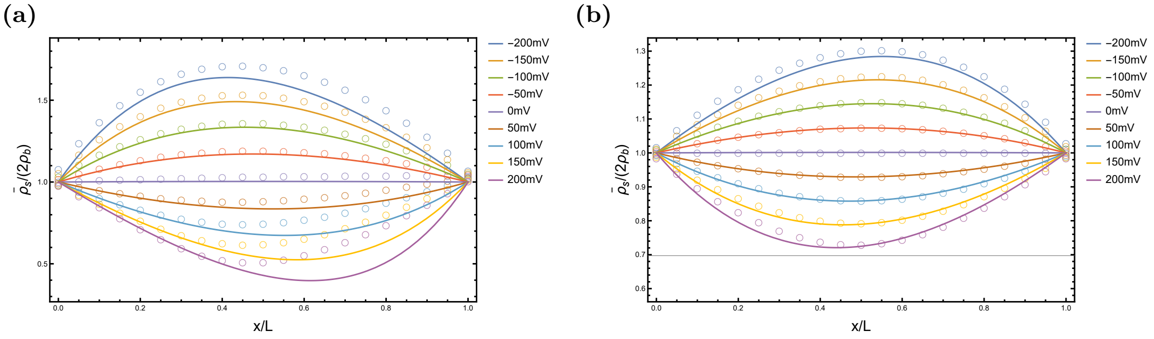

Figure 13: Radially average salt concentration profiles with AA and FE represented as solid lines and empty circles, respectively. The range of electric potentials for both systems are between $V \in [-200, 200]$ mV with the governing surface charge density being $e\sigma_0 = 0.5e\sigma_{ref}$. **(a)** The zero-point of the surface charge density is $x_0 = 0.3L$. **(b)** The zero-point of this channel is $x_0 = 0.7L$.

In Figure 13, we computed salt concentration profiles along the length of the channel for different surface charge density zero points. We compute this with the converged volume flow $Q_8(V)$ to ensure that we indeed have an accurately represented profile. The most evident difference between the two profiles, $x_0 = 0.3L$ seen in Figure 13(a) and $x_0 = 0.7L$ in Figure 13(b), is the increase in salt accumulation and depletion present in the $x_0 = 0.3L$. The reason this occurs is that to get $x_0 = 0.3L$ we are required to set $\sigma'/\sigma_0 = 10/3$. This is comparatively larger than $x_0 = 0.7L$ with $\sigma'/\sigma_0 = 10/7$. Thus with a larger surface charge density more accumulation and depletion may occur. We observe that due to the relatively larger surface charge density of $x_0 = 0.3L$, the analytical equations do not correlate to the same degree with the finite element calculation as $x_0 = 0.7L$. This reinforces our assumption that for larger surface charge densities our analytical equation does not operate to the same degree of accuracy.

We will now discuss the effect of flow on the salt concentration profiles. In Figure 13 we note that for a positive sloped volume fluid flows seen in Figure 11(b) as blue and yellow solid lines; the salt concentration profile will bias towards the base for negative electric potentials. The opposite is true for a negatively sloped volumetric flow in this case the salt concentration will be biased towards the tip for a negative electric potential. In Figure 11(b) we depicted the volumetric fluid flow as a function of the electric potential, for a negative electric potential $x_0 = 0.3L$ denoted in blue has a positive sloped fluid flow. The majority of the fluid is moving towards the zero point, indicating that the area of maximal salt accumulation will occur closer to the base of the channel. In comparison for $x_0 = 0.7L$ the slope of the volume fluid flow is negative which informs us that the maximal accumulation will be closer to the tip. Linking this to the profiles depicted in Figure 13 we see that our observation of positive and negative sloping volume fluid flow holds. Understandably, the accumulation would occur at the zero point in each case, it is interesting that there appears to be a reduced bias effect occurring for the maximal salt depletion as they are approximately maximal at half of the length of the channel. By increasing the electric potential the FE calculations provide more skewing away from the maximal accumulation of the channel which is captured by our analytical solution.

It is worth mentioning that the impact between $Q_0(V)$ and $Q_8(V)$ is negligible for both Figures 13(a) and 13(b). Furthering our discussion on the volume fluid flow effecting the salt concentration profile we will now discuss $x_0 = 0.5L$ where $Q(V) = 0$. In this case, the radially averaged salt concentration profile becomes parabolic with no bias occurring this can be seen in Figure 14.

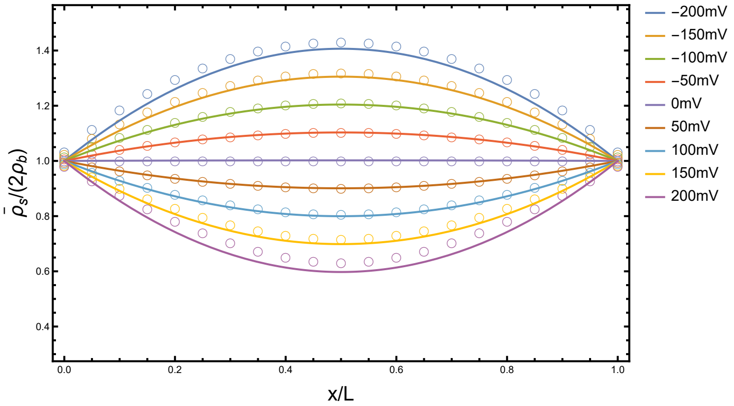

Figure 14: Salt concentration profile of a cylindrical channel with governing surface charge density of $e\sigma_0 = 0.5e\sigma_{ref}$ and zero point $x_0 = 0.5L$. AA is depicted as a solid line and FE are represented at empty circles, both ranging from $V \in [-200, 200]$ mV.

Remarkably, the fluid flows from the base and tip to meet in the centre of the channel. This is due to the surface charge density however, one can also say that the salt accumulation and depletion occurring in the system must be conducive to the annihilation of the volume fluid flow. Thus concludes our discussion on how the zero-point of the surface charge density influences the salt concentration profiles of cylindrical channels.

4 Diodic Behaviour in Cylindrical Channels

4.1 Diodic Behaviour

In this section, we will investigate the dependency of broken symmetries within a cylindrical channel that gives rise to diodic behaviour, i.e. current is only allowed to flow in one direction. An example of such a system is p-n junctions, which consist of a positive and negative silicone material. The p-type silicone is doped with boron gas to create a conductive material due to an excess of holes making it positive. The s n-type silicon is doped with phosphorous gas causing an abundance of electrons. The transfer of electrons from the negative side to the holes on the positive side creates a threshold electric potential to allow current to flow between the materials. The broken symmetry occurs within this material due to the depletion region forming [11].

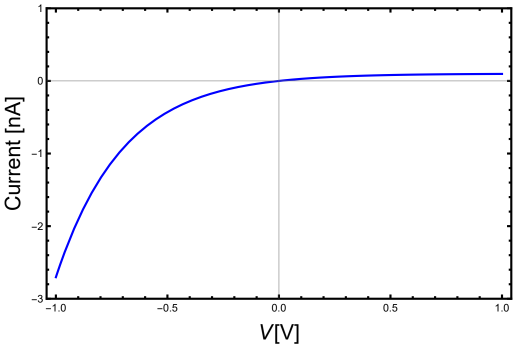

Figure 15: Diodic behaviour displayed using the Shockley diode [41] equation where we set the variables used in Eq. (4.1) to resemble the nature of ionic channels.

Figure 15 displays diodic behaviour modelled using the Shockley diode equation

$$I(V) = I_S \left(e^{\frac{V}{\eta V_T}} - 1 \right), \tag{4.1}$$

where $I(V)$ is the current, V is the voltage, $I_S = -0.1$ nA is the reverse bias saturation current, $V_T = -0.2$ V is the thermal voltage and $\eta = 1.5$ is the emission coefficient. This coefficient accounts for imperfections within the material that cause charges to cross the depletion region, when in an ideal diode it would not be possible [41]. If we apply a negative electric potential to the diode the current will flow freely. We have set the system parameters we used to resemble how ionic channels display diodic behaviour, which we will observe in later sections.

4.2 Diodic Behaviour in a Cylindrical Ionic Channel

The system we will be using for this section is a continuation of the model discussed in Section 3.2, where we have a cylindrical channel connecting two reservoirs with an inhomogeneous surface charge density applied to the walls of the channel. To model the diodic nature of an ionic channel we calculate the homogeneous channel conductance where no electric potential is applied to the the reservoir. To obtain this conductance we calculate the electric current using Eq. (2.38),

$$\begin{aligned} I(x) &= 2\pi e \int_0^R r \left(-D \left(\nabla\rho_+(x,r) + \rho_+(x,r)\frac{e\nabla\Psi}{k_BT} \right) + \mathbf{u}\rho_+(x,r) + D \left(\nabla\rho_-(x,r) - \rho_-(x)\frac{e\nabla\Psi}{k_BT} \right) - \mathbf{u}\rho_-(x,r) \right) \mathrm{d}r, \\ &\approx 2\pi e \int_0^R r \left(-D \left(\nabla\bar{\rho}_e(x) - \bar{\rho}_s(x)\frac{e\nabla\Psi}{k_BT} \right) + \mathbf{u}\bar{\rho}_e(x) \right) \mathrm{d}r. \end{aligned} \tag{4.2}$$

Similar to the total salt flux $J(x)$ 3.9, we approximate that ionic charge density, ρ_e, is only dependent on the lateral position along the channel i.e. $\rho_e(x,r) \approx \bar{\rho}_e(x) = \rho_+(x) - \rho_-(x)$. We assume that the ionic charge density is constant, therefore $\nabla\bar{\rho}_e(x) = 0$, and redefine $\bar{\rho}_s(x) = 2\rho_b$. Now the electric current can be computed as

$$\begin{aligned} I(x) &= 2\pi e \int_0^R r \left(2D\rho_b \frac{e\nabla\Psi}{k_BT} + \mathbf{u}\bar{\rho}_e(x) \right) \mathrm{d}r, \\ &= 2\pi D\rho_b \frac{e^2V}{k_BT}\frac{R^2}{L} + 2\pi e \int_0^R \mathbf{u}\bar{\rho}_e(x). \end{aligned} \tag{4.3}$$

Now we divide across by the electric potential to compute our conductance $g = I/V$, thus removing the dependency on the electric potential, fulfilling the condition of having the conductance across the channel without an applied electric potential. The static conductance with a constant salt concentration is then

$$g_0 = \frac{2\rho_b D e^2}{k_B T}\frac{\pi R^2}{L}. \tag{4.4}$$

We assumed that $\bar{\rho}_s = 2\rho_b$ to simplify the calculation of Eq. (4.3) [3, 46]. However, as we already know from Eq. (3.14), the salt concentration is not constant for an inhomogeneous surface charge density and depends on the position along the channel, and the electric potential. To incorporate the radially averaged salt concentration profile, we can treat the surface charge density as a series of resistors and thickness dx with cross-sectional area πR^2. Note that the electric field scales with the inverse of the square radius, therefore each slab gives a resistance of $(g_0\bar{\rho}_s(x, V)/2\rho_b)^{-1}\,\mathrm{d}x$ [18, 19]. The voltage-dependent channel conductivity is given by

$$g_\infty(V) = g_0\frac{L}{2\rho_b\int_0^L(\bar{\rho}_s(x, V))^{-1}\,\mathrm{d}x}, \tag{4.5}$$

where we normalized the slab over the channel as we are integrating the radially averaged salt concentration over the length of the channel. As we have removed the dependence on the position along the x-axis of the channel the remaining variable is the electric potential which causes non-linearity for the conductance. A current issue with this method of calculating the conductivity is that Eq. (3.14) can produce negative salt concentrations. While not depicted in Figure 6(b), for higher voltages our analytical approximation becomes unphysical. A method used by Kamsma et al. [18] is to replace $\bar{\rho}_s(x, V)$ with a condition which states that the salt concentration cannot be reduced past 10% of the bulk concentration. This takes into account the surface conductivity. Therefore, using this method where we no longer have negative salt concentrations, we can now model the steady-state current for a cylindrical channel as

$$I(V) = g_\infty(V)V. \tag{4.6}$$

4.3 The Effect of Charge Density Symmetries on Current-Voltage Behaviour

It has been found experimentally that current flowing through conical ionic channels is sensitive to pressure which was verified analytically by Boon et al. [3,16]. They found that this form of broken symmetry, regarding the pressure drop combined with an electric potential drop, indeed creates a more apparent diodic behaviour. This led to Kamsma et al. [18] incorporating a different form of broken symmetry, an inhomogeneous surface charge density across the conical channel wall. The surface charge density linearly changes along the length of the channel seen in Eq. (3.1). For a pictorial representation refer to Figure 6(a) where we plotted the surface charge density with respect to the length of the channel. They found that breaking the symmetry of the channel using Eq. (3.1) also aided in creating an unmistakable current rectification. The primary similarity in each study is that they had a broken symmetry always present in the form of the geometry being conical. In contrast to these works, where they considered a constant geometrical broken symmetry, we focus now on a cylindrical channel to probe if it is indeed a broken symmetry that gives rise to diodic behaviour. In doing so, we use the same theoretical model used in Section 3.2. We note here that the only broken symmetry present is that of the inhomogeneous surface charge Eq. (3.1). Inspecting the radially averaged salt concentration Eq. (3.14), note that the only remaining term of the surface charge density is σ' the term which causes the inhomogeneity. Therefore, by setting the surface charge density which provides the inhomogeneity to $\sigma' = 0$ we hypothesize that we do not achieve diodic behaviour. Instead, an Ohmic relation should emerge.

In the current-voltage relations in Figure 16 we have a governing surface charge density of $e\sigma_0 = e\sigma_{ref} = 0.1e$ nm^{-2}. In Figures 16(a) and 16(b) the surface charge densities are described by (3.1) with $\sigma' = 3/2\sigma_0$ and $\sigma' = 0$, respectively. It has been found experimentally that introducing a bipolar surface charge density to a cylindrical channel produces diodic behaviour [9,15,21]. In Figure 16(a) we have computed analytically using Eqs. (4.5) and (4.6) the current-voltage represented by the solid line and the numerical calculation denoted by empty circles. We note that this channel has strong current rectification that is accurately captured.

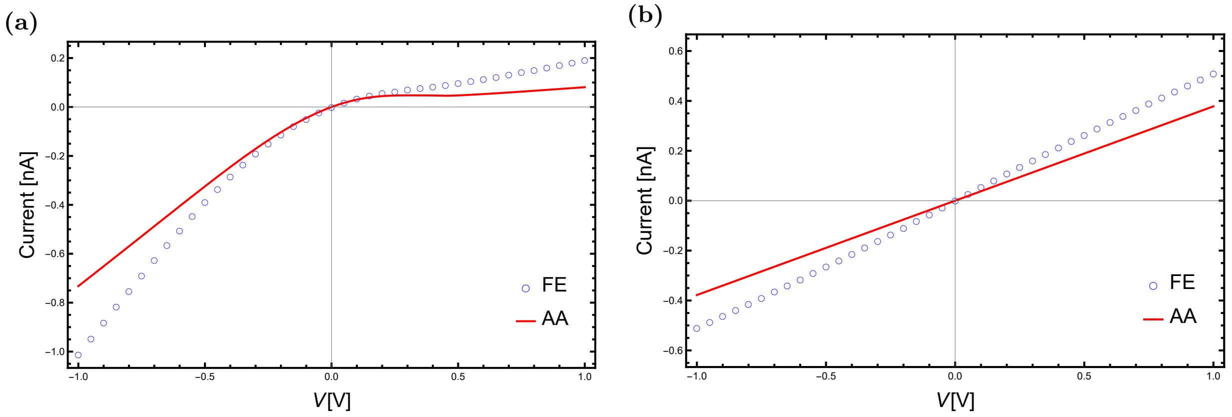

Figure 16: Current-voltage diagrams of cylindrical ionic channels with different σ' values for the change in surface charge densities, both channels have the same governing surface charge density $e\sigma_0 = 0.1e\ \mathrm{nm}^{-2}$. The solid line denotes the analytical approximation (AA) based on Eq. (4.6). The empty circles represent the finite element calculation (FE). **(a)** Inhomogeneous surface charge density applied to the walls of the cylinder using Eq. (3.16) $x_0 = 0.\dot{6}L$ producing a bipolar channel. **(b)** Homogeneous surface charge density, in this case, $\sigma' = 0$ thus, there is no zero point associated with this channel.

In looking at the current-voltage diagram of a perfectly symmetric cylindrical channel seen in Figure 16(b) where $\sigma' = 0$. Here we note that if we have a homogeneous surface charge across the channel we obtain an Ohmic relation in the current-voltage diagram. This means that for a cylindrical ionic channel, there is a dependence on a form of broken symmetry within the channel to obtain diodic behaviour. Specifically, the broken symmetry must cause an accumulation or depletion of salt concentrations. This symmetry relation has been noted in Ref. [14]. A pressure drop in combination with electro-osmotic flow has been investigated [47], and it was noted that the pressure drop can enhance the flow through the channel. Due to this enhancement of flow, we deduce that the addition of pressure could flush the ions from the channel, although further investigations are required to verify this statement.

A question may arise from this, why do we require an accumulation or depletion to occur within the channel to create this diodic effect? The reservoirs in our system are filled with an aqueous solution, specifically salt dissolved into the water. We may note that distilled water is not conductive to electrical current [13]. Therefore, we require the salt to aid in the conductance of the current. When the salt concentration depletes we are effectively reducing the conductance of the liquid within the channel. This emerges as diodic behaviour, inspecting Figure 6(b) we note the salt concentration depleting when in the positive regime which corresponds to the diodic behaviour seen in Figure 16(a). If we continue increasing the electric potential in Figure 6(b) past $V = 200$ mV we would have an area close to the centre of the channel where the number of ions present will not effectively allow for current to flow.

4.4 Time-Dependent Electric Potentials in a Cylindrical channel

We have discussed the steady-state nature of cylindrical ionic channels producing diodic behaviour. Now we will draw our attention to the time-dependent regime as an interesting phenomenon occurs. When a time-dependent electric potential $V(t) = V_0 \sin(\omega t)$ is applied in the reservoir far from the channel, with $V_0 = 1$ V and $\omega = 2\pi f$ with optimised frequency for most apparent memory effect, $f = 45$ Hz [19] we obtain a pinched hysteresis loop. As elaborated in Section 2.2, the pinched hysteresis loop is the hallmark sign of a memristor which has been found experimentally for cylindrical nanopores Ref. [35, 38]. To begin this investigation we first must understand why in certain cases microfluidic channels give rise to memristive properties.

In an ionic channel such as a cylindrical microfluidic system ions accumulate and deplete by a process of diffusion. Due to the diffusive nature of this system ion accumulation and depletion are not instantaneous, resulting in a characteristic timescale which retains the memory of the previous electric potential. We will derive an expression for this timescale taking inspiration from Refs. [18, 19]. We consider the total number of ions within the channel, recall the radially averaged salt concentration Eq. (3.14),

$$N = \pi R^2 \int_0^L \bar{\rho}_s(x)\,\mathrm{d}x.$$

We want to know the change in the number of ions due to a small voltage perturbation V' given by

$$\left.\frac{\partial N}{\partial V}\right|_{V=0} V' = \frac{\pi}{6} L \frac{eR\sigma'}{k_B T} V'. \tag{4.7}$$

The second term we require to formulate the characteristic timescale is the net salt flux (2.39) into the channel with a small voltage perturbation,

$$\left.(J_x(0) - J_x(L))\right|_{V=0} V' = 2\pi \frac{eDR\sigma'}{k_B T L} V'.$$

Taking the ratio of the rate of change of the number of ions in the channel due to a small perturbation V', and the net salt flux through the channel with the same perturbation we arrive at our diffusive timescale,

$$\tau = \frac{L^2}{12D}. \tag{4.8}$$

We can note from Ref. [19] that the conical channel maintains this diffusive timescale for both homogeneous and inhomogeneous surface charge densities. However, for a cylindrical channel as we have seen in Figure 16(b) of the Ohmic response observed in the current-voltage diagram. If we impose a homogeneous surface charge density i.e. $\sigma' = 0$, no salt accumulation and depletion occurs, thus there is no dependence on past states. For an inhomogeneous surface charge density, $\sigma' \neq 0$, we obtain at the same time scale as the conical channel. Therefore, the geometry does not play a role in the time scale.

Now that we have formulated the diffusive timescale. We want to create an equation that incorporates this diffusive effect with a conductance that is time and voltage-dependent such that we have a current-voltage equation of the form,

$$I(V) = g(V(t), t)V(t), \tag{4.9}$$

where $g(V(t), t)$ is the memductance, dependent upon the electric potential $V(t)$ applied to the reservoir of the system far from the channel and the time t. To compute the memductance, we assume that the rate of change of the memductance with respect to time is proportional to the difference between the steady-state memductance and the time-dependent memductance. This assumption has proven to be effective in Refs. [18, 19, 27, 37]. Thus the memductance is of the form

$$\frac{\partial g(V(t), t)}{\partial t} = \frac{g_\infty(V(t)) - g(V(t), t)}{\tau}. \tag{4.10}$$

Using this, we evaluate the current-voltage diagram seen in Figure 17 for a time-dependent electric potential. We have used the same parameters used to create the diodic behaviour from Figure 16(a) where $x_0 = 0.\dot{6}L$.

We see that our AA solution accurately captures the hallmark memristive property of a pinched hysteresis loop and is in good agreement with our numerical calculation FE. This informs us that using the radially averaged salt concentration to compute the time-dependent memductance is an accurate predictor for the current-voltage diagram for a cylindrical channel. We note that a cylindrical channel with a homogeneous surface charge density and an applied time-dependent electric potential gives an Ohmic response for the current-voltage diagram and is the same as Figure 16(b).

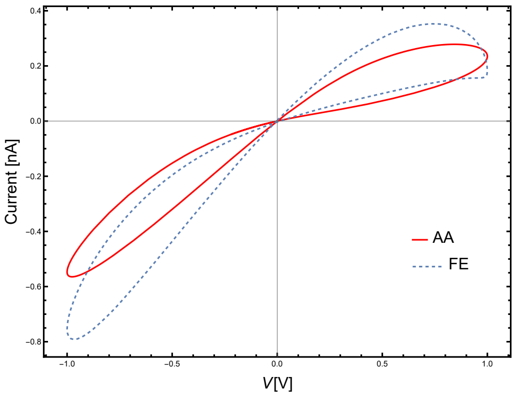

Figure 17: Comparision between analytical (AA) and finite element (FE) calculations denoted by a solid line and a dotted line, respectively. Current-voltage diagram of a cylindrical BP channel where a time-dependent voltage is applied to the reservoir. The electric potential is $V(t) = V_0 \sin(\omega t)$, where $V_0 = 1$ V and $\omega = 2\pi f$ where $f = 45$ Hz the optimal frequency [19]. We use the same parameters used to create Figure 16(a) where the zero-point of the channel is $x_0 = 0.\dot{6}L$ with governing surface charge density $e\sigma_0 = 0.1e$ nm^{-2}. The diffusive timescale for these parameters is $\tau = 4.\dot{2}$ ms with $2\pi f\tau = 1.19$ for an optimal memory effect [18, 19].

5 An Investigation of Conical Ionic Channels

5.1 Conical Channels

Up to this point, we have delved into the nature of cylindrical channels, and how to formulate the set of PNPS equations to model the volumetric flow and diodic behaviour. With the final investigation, we have shown that such a channel can produce memristive behaviour providing we have a broken symmetry in the form of an inhomogeneous surface charge density. Now we will look toward a different geometry as a special case, that of a conical channel.

Figure 18(a) is a schematic diagram which we will be using for the basis of this section with the electric driving force depicted in Figure 18(b) where an applied static electric potential is applied to the reservoir located at $x = -\infty$ nm. The red dotted lines indicate the channel in Figure 18(b). We will be

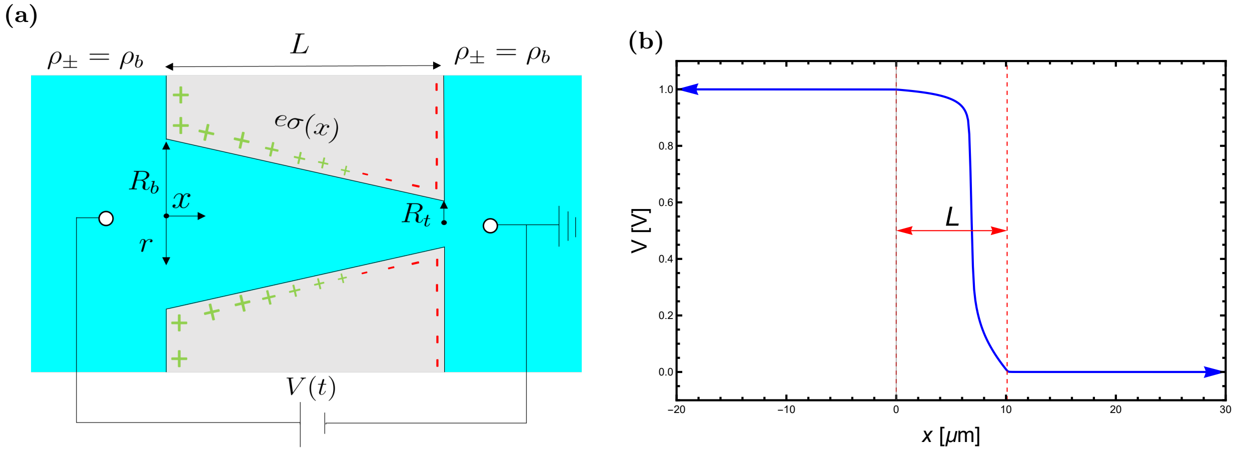

Figure 18: **(a)** Schematic representation of an axially symmetric bipolar (BP) conical channel [18], with channel length L, radius $R(x)$ expressed in Eq. 5.1. The channel connects two bulk reservoirs of 1:1 electrolytes with bulk concentration ρ_b. Along the channel surface, there is a surface charge density $e\sigma(x)$, where we used Eq. (3.1). An electric potential, $V(t)$ is applied to the bulk reservoir at an infinite distance from the channel on the left-hand side and then grounded in the opposite reservoir. **(b)** Finite element calculation of the electric potential drop across the conical channel. The channel is represented as residing within the red dotted lines with an applied voltage of $V = 1$ V.

using the same parameters used to establish the cylindrical channel in Section 3.2, this was developed upon Ref. [3, 18, 19, 22, 29]. With the notable exception that the base radius $R_b = 200$ nm and the tip radius $R_t = 50$ nm [23] and is described by

$$R(x) = R_b - \Delta R\frac{x}{L}, \tag{5.1}$$

where $\Delta R = R_b - R_t$. Using this new geometry we will update the radially averaged salt concentration which was evaluated in Ref. [18] for a BP conical channel,

$$\bar{\rho}_s(x,V) = 2\rho_b - \frac{1}{\mathrm{Pe}/V}\frac{2e(\sigma_0\Delta R + \sigma' R_b)}{k_BTR_t^2}\left(\frac{R_b(1-x/L)}{R(x)} - \frac{e^{-\mathrm{Pe}(1-x/L)\frac{R_t}{R(x)}} - 1}{e^{-\mathrm{Pe}\frac{R_t}{R_b}-1}}\right). \tag{5.2}$$

Here, the Péclet number is composed differently than the cylindrical channel to incorporate the conical geometry, $\mathrm{Pe} = Q(V)L/\pi DR_t^2$. Where the volumetric flow is formulated as

$$Q(V) = -\frac{\pi R_b R_t \varepsilon\psi_{eff}V}{\eta L}. \tag{5.3}$$

Here $\psi_{eff} = -25$ mV is the effective surface potential fitted to the finite element calculation. The effective surface potential is a way to ensure that the volume flow is accurately captured for this conical channel with the initial surface charge density $e\sigma_0 = e\sigma_{ref} = 0.1e$ nm^{-2} and zero-point $x_0 = 0.\dot{6}L$. Let's briefly discuss the electro-osmotic mobility $-\varepsilon\psi_{eff}/\eta$. This mobility describes how freely the fluid can flow through the channel with an applied surface potential. Therefore, if the flow is hampered it will occur due to this ratio, we now observe the surface potential along the channel.

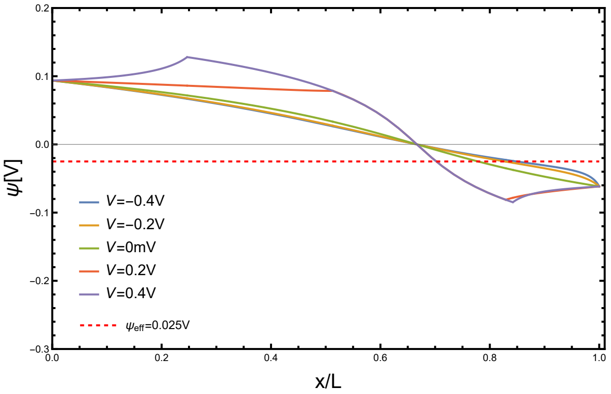

Figure 19: Analytically approximated surface potential along the length of the channel. The governing surface charge density is $e\sigma_0 = e\sigma_{ref} = 0.1e$ nm^{-2} with a zero point $x_0 = 0.\dot{6}L$. We compute the surface potential for static electric potentials in the range $V \in [-0.4, 0.4]$ V indicated by the solid lines. The dotted red line indicates the effective surface potential.

Figure 19, describes the surface potential along the length of the channel with a governing surface charge of $e\sigma_0 = e\sigma_{ref}$ and zero-point $x_0 = 0.\dot{6}L$. We calculated the analytically approximated surface potential with the inclusion of the effective surface potential seen as a dotted red line. Observing 19 we have a noticeably larger positive surface potential located close to the base of the channel compared to the negative potential at the tip. We note that the surface potential exists only in the channel itself and tends to zero when we look into the reservoir for $x < 0$ and $x > L$. This is due to the nature of the charge density. If there is no surface for a charge density to be implemented there is no surface potential either. This is assumed as a boundary condition. We now inspect the volumetric flow through the channel.

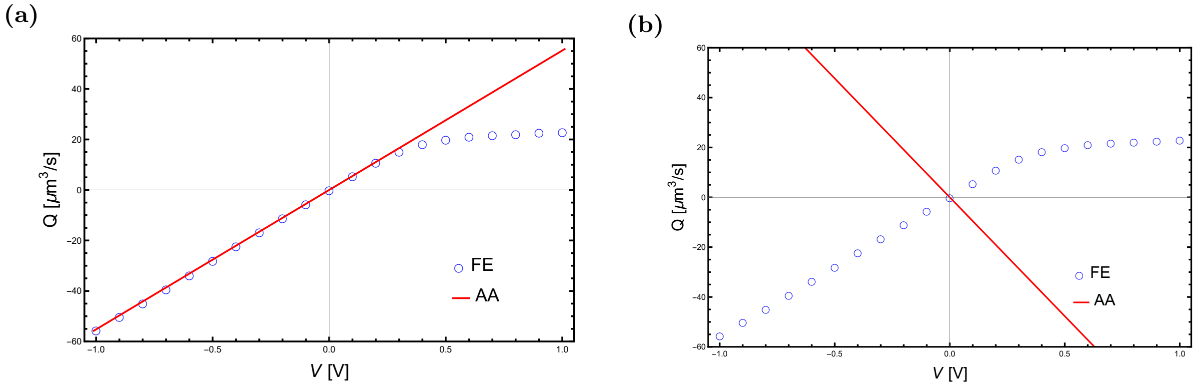

Figure 20: Volume fluid flow plotted against the static electric potential diagrams with finite element (FE) and analytical approximation (AA) described by blue empty circles and a solid red line, respectively. **(a)** An effective surface potential was used where $\psi_{eff} = -25$ mV such that we achieve a good agreement with the linear part of this diagram. **(b)** We used the Gouy-Chapman surface potential. Eq. (3.18), for the volumetric flow Eq. (5.3). The laterally averaged surface potential is $\bar{\psi} = 43$ mV.

Figure 20(a) describes a volumetric flow as a function of the static electric potential V. We have fit a line to the volumetric fluid finite element calculation denoted by empty circles to create an effective potential ψ_{eff}. This contrasts with the method used for the cylindrical channel where we have used the Gouy-Chapman surface potential seen in Figure 20(b). The Gouy-Chapman method does not correlate to the FE numerical analysis. This potentially means that the geometry of this system produces a weighted effect closer to the tip of the channel. We will further discuss this topic in Section 5.3.

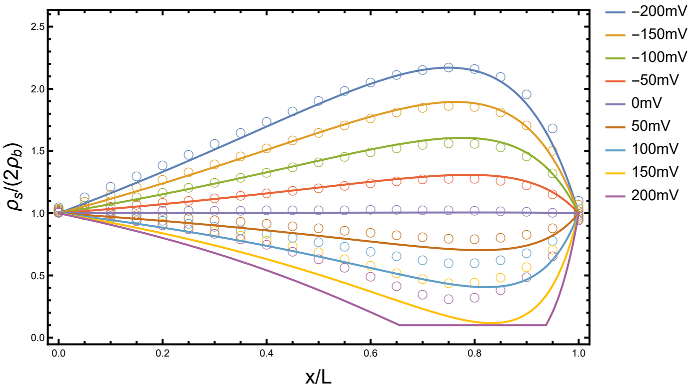

Figure 21: Conical channel salt concentration profile where the governing surface charge density is $e\sigma_0 = e\sigma_{ref}$ and zero-point $x_0 = 0.\dot{6}L$. The electric potential range is $V \in [-200, 200]$ mV with the FE analysis denoted by empty circles and AA represented by solid lines.

We will discuss the radially averaged salt concentration seen in Figure 21. We used the effective potential ψ_{eff} to produce the radially averaged salt concentration spanning the length of the channel seen in Figure 20(a). We note that the analytical approximation has a good agreement with the finite element calculation for negative electric potentials. However, as we move to positive electric potentials the agreement becomes worse with each increase in 50 mV. The ad-hoc method of creating an effective cut-off point for the salt concentration profile is used due to the unphysical nature of having a negative salt concentration. We see in Figure 21 that for $V = 200$ mV we have set the salt concentration to 10% of the bulk of the analytical approximation reduces to a value below that cut-off [18]. If we compare the salt concentration profile of the conical channel in Figure 21, to that of a cylindrical channel in Figure 6(b). Where both have the same inhomogeneous surface charge density, the effect of the narrow tip radius on the salt concentration profile becomes readily apparent. The maximal and minimal concentrations reside close to the tip of the channel for a cone. Comparatively, the cylindrical channel's maximal accumulation and depletion are approximately located at the zero-point of the surface charge density on the channel.

5.2 Ohmic Relation

We will now turn our focus to the radially averaged salt concentration Eq. 5.2 for a conical channel. It is already known from Refs. [3, 18] that such an equation can provide diodic behaviour for both an inhomogeneous BP channel and a homogeneous unipolar channel i.e. $\sigma' = 0$. We note that there is a prefactor involved within Eq. (5.2) which may control the diodic nature of a conical channel with an inhomogeneous surface charge density applied to the system's walls. Setting this prefactor to zero we have,

$$\sigma_0 \Delta R + \sigma' R_b = 0. \tag{5.4}$$

If this prefactor is equal to zero we will obtain an Ohmic relation. We will first reformulate the equation to be a dimensionless equation to gain a deeper understanding of how Ohmic behaviour emerges within a conical channel,

$$\frac{R_t}{R_b} - \frac{\sigma'}{\sigma_0} = 1, \tag{5.5}$$

here we have rearranged Eq. (5.4). We note that any value that satisfies Eq. (5.5) creates an Ohmic current-voltage diagram. Let's delve further into Eq. (5.5), providing that $R_b > R_t$ for a conical channel. This means that the ratio of the tip and base radii will be in the range $\frac{R_t}{R_b} \in (0, 1)$. Therefore, the dimensionless ratio is in the range $\frac{\sigma'}{\sigma_0} \in (-1, 0)$ to create a linear current-voltage relation. Inspecting the dimensionless surface charge density ratio, we find that $-\sigma_0 < \sigma' < 0$, meaning that we never achieve a bipolar channel, only an inhomogeneous unipolar channel. We can deduce this by noting that to achieve a bipolar channel $\sigma' < -\sigma_0$, but as stated $\sigma' > -\sigma_0$ must hold to provide an Ohmic response, thus a bipolar channel cannot occur. We cannot use Eq. (3.16), which has a zero-point x_0 because of this unipolarity.

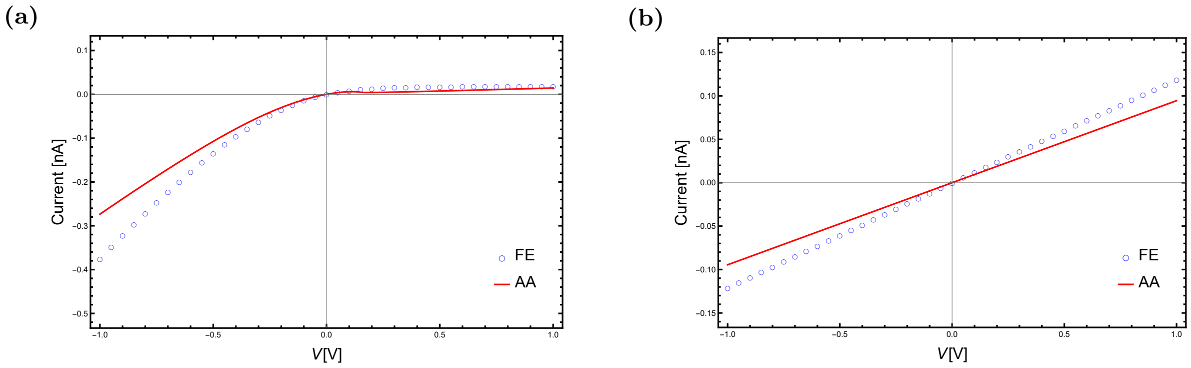

Figure 22: Static current-voltage diagrams of conical channels with the same base and tip radii $R_b = 200$ nm and $R_t = 50$ nm. The surface charge density is described by $\sigma(x) = \sigma_0(1 - \sigma'/\sigma_0 x/L)$ with the governing surface charge density being $e\sigma_0 = e\sigma_{ref} = 0.1e$ nm^{-2}. Finite element (FE) analysis is denoted by the blue empty circles and the analytical approximation (AA) is represented by the solid red line. **(a)** We set $\sigma' = -3/2\sigma_0$ to produce diodic behaviour. **(b)** Here we used (5.5) to create an Ohmic relation by setting $\sigma' = -3/4\sigma_0$.

In Figure 22 we have depicted current-voltage diagrams, where two behaviours emerge from purely the surface charge densities varying. We have set for both channels the base and tip radii to be $R_b = 200$ nm and $R_t = 50$ nm, respectively with the same governing surface charge density $e\sigma_0 = e\sigma_{ref} = 0.1e$ nm^{-2}. The purpose of this is to have an honest comparison between the channels. In Figure 22(a), we set $\sigma' = -3/2\sigma_0$, which provided us with a very apparent diodic behaviour present in the current-voltage diagram. This compares to Figure 22(b) where we set $\sigma' = -3/4\sigma_0$ to satisfy Eq. (5.5). In doing so, we create an Ohmic current-voltage diagram. An interesting factor to note is that we have seen from Ref. [3] that a homogeneous unipolar channel produces diodic behaviour. However, with the correct ratio of the surface charge density,

σ'/σ_0. We can remove the salt accumulation and depletion from occurring within the channel. This provides a homogeneous salt concentration profile of approximately the bulk $2\rho_b$ for all electric potentials applied to the reservoir.

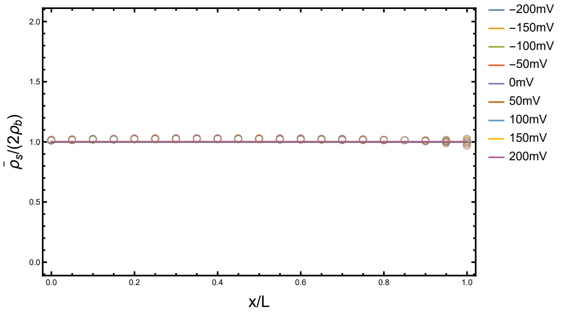

Figure 23: Conical channel salt concentration profile where the governing surface charge density is $e\sigma_0 = e\sigma_{ref}$ with $\sigma' = -3/4\sigma_0$ such that we have an Ohmic current-voltage relation seen in Figure 22(b). The finite element (FE) calculation is represented by empty circles and the analytical approximation (AA) is denoted by a solid line. The range of electric potential is $V \in [-200, 200]$ mV.

In Figure 23, we plot the radially averaged salt concentration across the length of the channel. We note that the salt concentration profile is approximately constant for any applied voltage for the parameter choice used in 22(b). As no accumulation or depletion occurs in this case the conductivity remains constant providing the Ohmic response. This creates an Ohmic relation as seen in Figure 22(b). Furthering this investigation, we note that for an accumulation in salt concentration, we have an increase in conductance. Therefore, comparing the values of current at $V = -1$ V there is a difference of approximately $\Delta I = -0.3$ nA. When there is a depletion there is close to no current flowing in the diodic case 22(a) compared to $\Delta I = 0.1$ nA for the Ohmic channel. Thus to obtain diodic behaviour a depletion of ions must occur within any channel, which when the system moves to a time-dependent regime memristance occurs due to the time delay between depletion and accumulation causing a pinched-hysteresis loop.

5.3 Volumetric Flow Analysis

In this section, we will investigate the phenomenology of volumetric flow in conical channels. We have been unable to create a self-contained set of equations which can describe a conical ionic channel. Due to this, we have kept the effective surface potential as a fitted parameter seen in volumetric flow Figure 20(a). The reason can be noted in Figure 20 where the known method for a cylinder was used and did correlate with the volume fluid flow finite element calculation. To understand what is occurring within the channel we will take two approaches, the first where we apply a weight to the Gouy-Chapman surface potential. In the second approach, we will inspect purely the negative electric potentials to see if any patterns arise giving further information on the nature of a conical channel. We note that our cylindrical model with the best success with relatively high surface potentials was for $e\sigma_0 = 0.5e\sigma_{ref} = 0.05e$ nm^2 seen in the volumetric flow diagram of a bipolar cylindrical channel, Figure 11(b).

5.3.1 Weighing the Gouy-Chapman Surface potential

We examine a method to weigh the laterally averaged surface potential such that we have a positive slope as depicted in the volumetric flow diagram of a conical bipolar channel, Figure 20(a). When inspecting the effective surface potential which has a fitted value of $\psi_{eff} = -25$ mV. If we take the lateral average of the last third of the channel we have $\bar{\psi} = -34$ mV [18], which is remarkably close to effective potential. This means that the geometry weighs the tip of the channel to be more dominant than the rest of the surface potential on the channel. The range of the surface potential is $\psi \in [92, -61]$ mV where the first surface potential value is the surface potential at the base and the latter is at the tip.

The weighted laterally averaged surface potential will be of the form,

$$\bar{\psi}(V) = \frac{1}{\mathcal{N}} \int_0^L w(x) \left(\frac{2k_B T}{e} \right) \sinh^{-1}(2\pi\lambda_D\lambda_B\sigma(x))\, \mathrm{d}x. \tag{5.6}$$

Where $w(x) = 2\pi R(x)^i$ is the weight which is applied to the lateral average, to vary the weight we have the power i, $\mathcal{N} = \int_0^L w(x)\, \mathrm{d}x$ is the normalisation factor. If our conical channel has radii $R_b = 200$ nm and $R_t = 50$ nm for the base and tip, respectively, we want the power i to be negative so that the tip will be more dominant. To begin we will look at various channels with different tip radii, going from a cylindrical channel, which we know is successful at providing a good agreement in the linear case, to the standard conical channel of 50 nm. We will inspect two BP surface charge densities which have previously provided good linear agreements to the finite element calculation, which are represented by the zero-points $x_0 = 0.7L$ and $x_0 = 0.6L$.

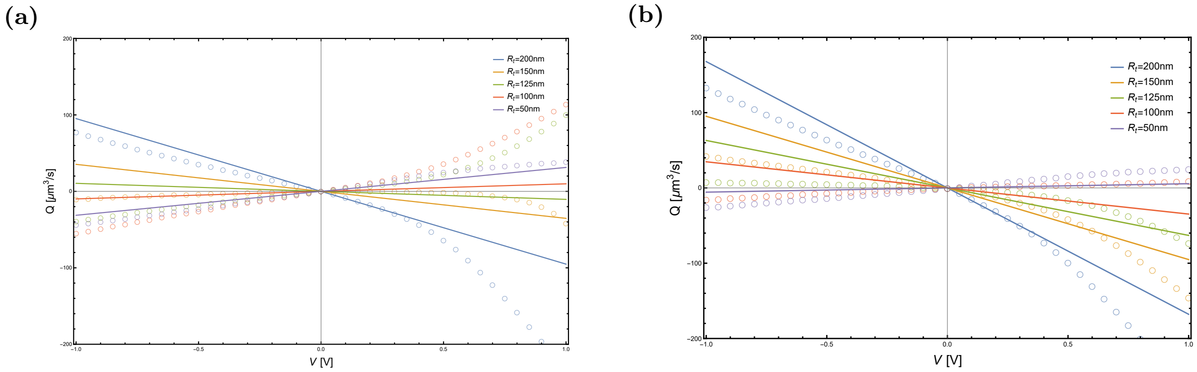

Figure 24: Volumetric flow diagrams as a function of applied static electric potential with the weighted function to the power of $i = -2$. We vary the radii of the tip of the channel as indicated by the colours in the diagram. The FE analysis is denoted by empty circles and the solid lines are AA analysis. The governing surface charge density for all cases is $e\sigma_0 = 0.5e\sigma_{ref}$. In **(a)** the zero point is located at $x_0 = 0.6L$, and **(b)** is located at $x_0 = 0.7L$, for varying tip radii.

Figure 24 depicts the volumetric flow as a function of the steady-state voltage V, we have set the weight power to $i = -2$ to observe what occurs to our analytical approximation. We note that weighing the laterally averaged zeta potential we do not fully capture the turning point at which the flow goes from negative to positive for varying the tip radius of the channel. To capture this turning point we gradually decrease the power i until we obtain the desired pivoting effect from negative to positive flow.

We arrive at the final power of $i = -4.5$. In Figure 25 of the volumetric flow plotted with respect to the electric potential, we see that the flow is in good agreement with the turning point. This is noted as we capture the volume fluid flow negative electric potentials. Figures 25(a) and 25(b) are volumetric flow diagrams plotted against the static electric potential V. Here we use the same governing surface charge density $e\sigma_0 = 0.5e\sigma_{ref}$ for zero-points $x_0 = 0.6L$ and $x_0 = 0.7L$, respectively. There is no apparent reason as to why $i = -4.5$ should provide a good agreement to the finite element calculation. Therefore, for now, we will only view this as a phenomenological result that could be coincidental and not provide a good method of representing the volumetric flow of conical channels. One can note that for a cylindrical channel, the weighted function does not affect the surface potential as we have set $w(x) = 2\pi R(x)^i$. In the case of the cylinder, the radius is constant making the weight redundant. This works well for our analytical approximations as we know that the cylindrical channel can be accurately modelled without a weight applied to the zeta potential.

We assumed that if we applied a weight to the Gouy-Chapman surface potential we would arrive at a well-functioning volume flow equation. To test this assumption we use the best case that we have seen thus far, that of the weight with the power $i = -4.5$. We will use the iterative method described by Figure 9(a) on this weighted function.

In Figure 26 we compute the volumetric flow with respect to the static voltage V. We implemented the

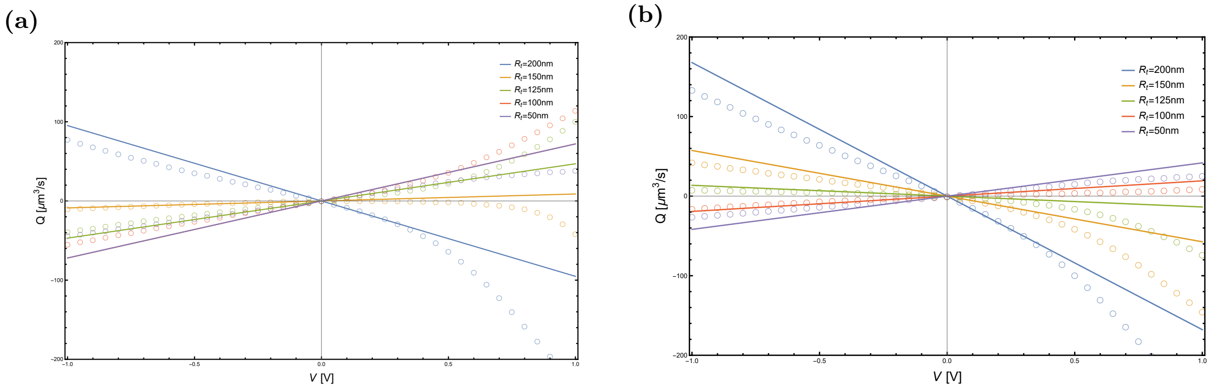

Figure 25: Volumetric flow diagrams with the weighted function having an index of $i = -4.5$ computed as a function of an applied time-independent electric potential V. The FE analysis is denoted by empty circles and the solid lines are AA analysis. The governing surface charge density for all cases is $e\sigma_0 = 0.5e\sigma_{ref}$. In these diagrams, we keep the zero-point constant and vary the radii. **(a)** These are BP channels with $x_0 = 0.6L$ for varying tip radii. **(b)** These are BP channels where the zero-point is $x_0 = 0.7L$ for varying tip radii.

iterative method up to eight iterations. We use the governing surface charge density of $e\sigma_0 = 0.5e\sigma_{ref}$ for a zero-point $x_0 = 0.7L$. The base and tip radii are 200 nm and 50 nm, respectively. We note that the negative potential has a good agreement with our eighth iteration of the volume flow equation. Unfortunately, due to the nature of the Gouy-Chapman equation being an inverse sine hyperbolic function, the flow begins to increase. This indicates that we must alter the laterally averaged Gouy-Chapman surface potential such that we achieve the desired effect. This is purely following the phenomenology which does not inform us of the nature of the system. It does not provide a reason as to why the volume fluid flow is behaving in this manner due to the change in geometry. As we have a method of capturing flow for negative electric potentials we wish to understand this regime in more detail.

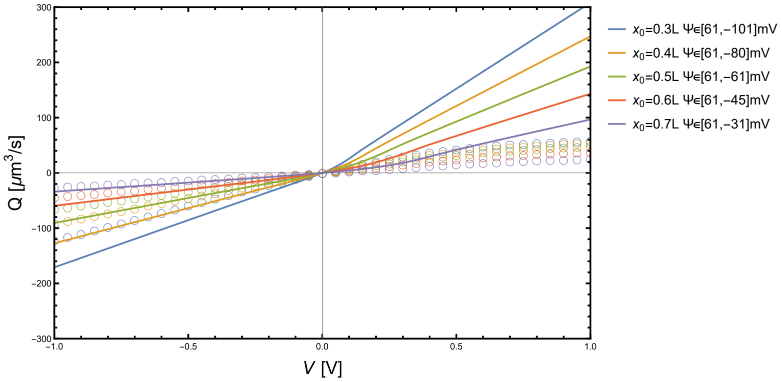

Figure 26: Comparison between FE and AA calculations denoted by empty circles and solid lines, respectively. The governing surface charge density is $e\sigma_0 = 0.5e\sigma_{ref}$ with the base radius being $R_b = 200$ nmand the tip being $R_t = 50$ nm. Calculated the volumetric flow to the eighth iteration to provide the analytical solution while varying the zero-point of the bipolar conical channel.

5.3.2 Analysing Negative Electric Potentials

In this subsection, we will analyse the purely negative electric potentials depicted in the volume fluid flow diagrams. The reasoning is that the negative electric potentials yield essentially linear flow-voltage relation. Thus we assume that after a detailed analysis of the negative electric potentials we can model the nature of the negative volumetric flow accurately. If we can model the linear flow perhaps we may be able to apply the same methodology used in Section 3.4 to produce the non-linearity present in the positive electric potential regime.

To begin this analysis we fit the volume fluid flow to the finite element calculation points so that we can obtain the effective surface potential for different values of R_t. We set the governing surface charge density to be $e\sigma_0 = 0.5e\sigma_{ref}$. Figure 27 depicts the use of effective electric potentials to fit with the finite element calculations in a flow-voltage diagram. Each line refers to a different tip radius in the range $R_t \in [50, 200]$ nm. The governing surface charge density is $e\sigma_0 = 0.5e\sigma_{ref}$ with the zero point $x_0 = 0.7L$. We repeated this process for various zero-points from $x_0 = 0.3L$ to $x_0 = 0.7L$ increasing the zero-point by $0.1L$ each time.

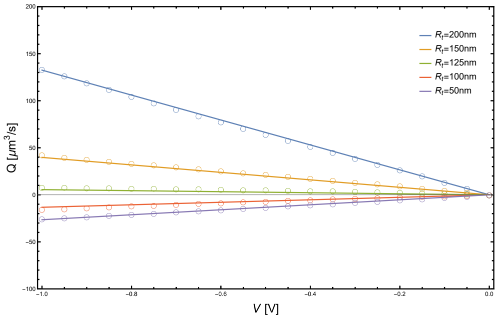

Figure 27: Flow-voltage curves for base radius $R_b = 200$ nm and various tip radii R_t for a bipolar channel with charge density $\sigma(x) = \sigma_0(1 - x/x_0)$. The governing surface charge density is $e\sigma_0 = 0.5e\sigma_{ref}$ with a zero point located at $x_0 = 0.7L$. We create an effective surface potential for every R_t to fit the volume fluid flow, represented by solid lines, to the finite element calculation denoted by empty circles.

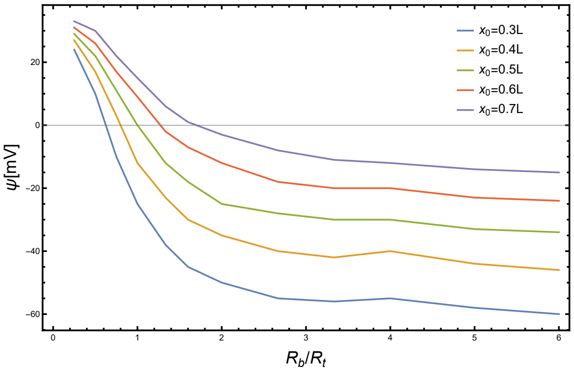

Figure 28: Effective surface potentials obtained from 27 plotted as a function of the ratio between the base and tip radii, respectively. This was completed using a governing surface charge density of $e\sigma_0 = 0.5e\sigma_{ref}$ for different zero points ranging from $x_0 \in [0.3L, 0.7L]$ as indicated by the colours in the diagram.

In Figure 28, we plotted the ratio of the base and tip radii against the effective zeta potential for different surface charge density zero points. We note that there appears to be a singular point which all zero points tend towards when the ratio is $R_b/R_t < 1$. In previous sections, we set our theory such that $R_b \geq R_t$. For this analysis, we allowed for the base to be smaller than the tip to observe if we were dealing with an asymptote. This is primarily because, for a larger ratio, the curves appear to plateau. Inspecting the effective potentials in the region of $R_b/R_t < 1$ we are reminded that for each of these zero-points, the initial surface charges are all the same $0.5\sigma_0$. Thus when we make the base smaller than the tip we weigh the base more. Due to all the channel bases having approximately the same surface charge densities all the curves appear to converge to the same surface potential $\psi_{eff} \approx 25$ mV. For $R_b/R_t > 1$ we see the opposite happening as the tip surface potential is weighted more than the base. Interestingly, if we continue to increase the ratio the surface potential begins to plateau. From this, we deduce that the weight doesn't become more refined to a smaller area close to the tip. What is truly remarkable is that for each zero point, the shape of each curve appears to be of a similar pattern.

Furthering our investigation of how to model the volumetric flow, we plot the effective surface potential against the surface charge density zero points for different ratios depicted in Figure 29.

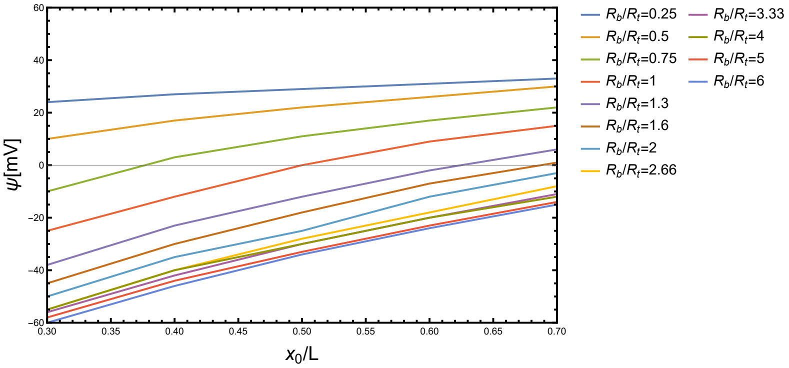

Figure 29: Effective surface potential plotted as a function of the dimensionless zero-point x_0/L for varying ratios of base and tip radii as indicated by the coloured solid lines. The data was obtained by fitting the volumetric flow as depicted in 27. The governing surface charge density for all bipolar channels is $e\sigma_0 = 0.5e\sigma_{ref}$.

Figure 29 we have an effective surface potential plotted with respect to the charge density zero point x_0/L. Here we can note that each curve appears to be effectively linear. This shows promise for creating a model of the volume flow as it informs us that the equation is decoupled. In other words, there is no interaction between variables and it can be solved independently. After $R_b/R_t = 2$ seen in Figure 29 the curves meld into one and there is little variance between $R_b/R_t \geq 2.66$. This coupled with a similar observation seen in Figure 28 tells us that the area of the channel which is most dominant doesn't change drastically. We expect the same to occur for ratios $R_b/R_t < 0.25$. The reason is that the system should reach a maximal weight around the base of the channel at this point.

Inspecting Figures 28 and 29 where we depict the surface potential as a function of the ratio of R_b/R_t and zero-points, respectively. We can deduce that there is a region which dominates the surface potential within the channel as we would have expected the distances between each line to be quasi-equidistant, specifically for Figure 29. Due to this minimal difference, we assume that the geometry no longer plays a modifying role in moving the dominant region as it has reached an ideal area for salt to accumulate and deplete.

5.3.3 Analysing the Debye Length for a Conical Channel

Calculating the Debye length using the radially averaged salt concentration, we find approximately that $\lambda_D \in [5, 22]$ nm, where the former is for negative electric potentials and the latter is for positive. There is a notable restriction region in which the fluid is free to flow outside of the effect of the surface potential. We originally assumed that $R(x) \gg \lambda_D$ which was true for a constant salt concentration. However, as we move into the positive electric potentials this no longer begins to hold as we go from $R_t/\lambda_D \approx 10$ to $R_t/\lambda_D \approx 2$. This in turn may provide a reason as to why we have been unable to calculate the volume flow within a reasonable agreement of finite element calculations. To test this we look at a cylindrical channel of 50nm seen in Appendix B. The cylindrical channel is known to provide good results for a radius of 200 nm, which is why we investigate a channel of 50 nm. We note that the volumetric flow is not correlated to the finite element calculation. It becomes apparent that it arises due to the Debye length being much larger than the radius of the channel. Returning to the discussion of the conical channel we will compute the Debye length along the surface of the channel.

Figures 30 describe the nature of the Debye length along the length of the channel. The Debye length was superimposed over a conical channel to aid our understanding of the Debye length located on the channel wall. The solid black line denotes the channel wall and the dotted black line informs us of the centre of the channel. The governing surface potential in Figures 30 is $e\sigma_0 = 0.5e\sigma_{ref} = 0.05e\ \text{nm}^{-2}$. Figure 30(a) we set the zero point to be $x_0 = 0.3L$, and Figure 30(b) is $x_0 = 0.7L$. We observe that for positive electric potentials, the Debye length becomes substantially larger than what we previously assumed. The apparent plateau seen in 30(a) occurs due to the condition that does not allow for negative salt concentrations. As we are no longer in the regime of $\lambda_D \ll R(x)$ we return to the original equation for the volumetric flow (3.12). We assumed that the first term in this equation was dominant and neglected the second term. Due to this,

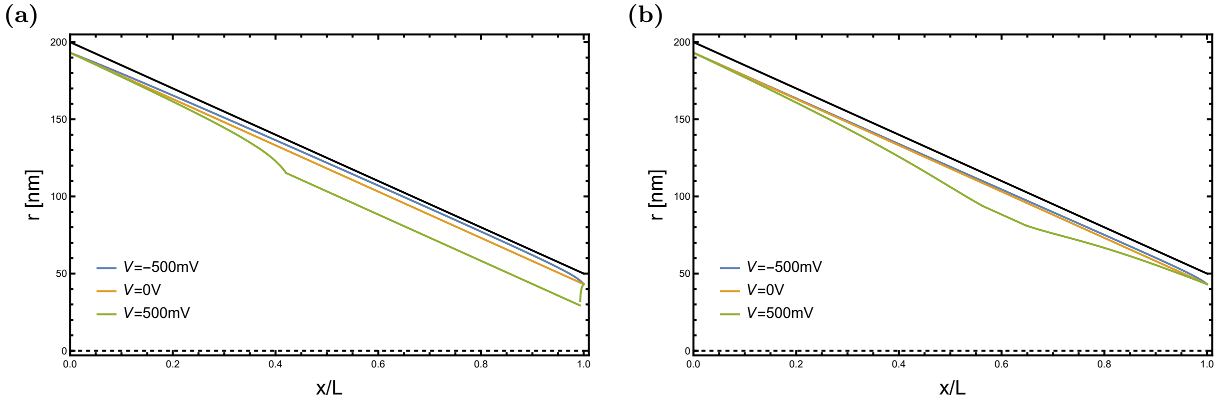

Figure 30: Debye Length imposed along the length of bipolar conical channels denoted by coloured lines displayed by plotting $R(x) - \lambda_D(x, V)$. The governing charge density is $e\sigma_0 = 0.5e\sigma_{ref} = 0.05e$ nm^{-2}. The dotted black line denotes the centre of the channel and the solid black line the channel wall. We calculate the Debye length using Eq. (3.17) for static electric potentials ranging from $V = [-500, 500]$ mV. The zero points depicted are **(a)** $x_0 = 0.3L$, and **(b)** $x_0 = 0.7L$.

we believe that to solve for conical volumetric flow the Debye length must play a more involved role. This concludes our analysis of the phenomenology of volumetric flow in a conical channel.

6 Summary and Outlook

In this thesis, we investigated the microfluidic transport through ionic channels. We first concerned ourselves with a perfectly symmetric geometry, that of a cylindrical channel with a radius of 200 nm. We assumed an inhomogeneous surface charge density was applied to the walls of the channel and applied a static electric potential drop across the system. This created a fascinating non-linear behaviour in the flow-voltage diagram. We reviewed the inhomogeneous charge density equation to provide an easy method of distinguishing between different charge densities. In doing so we created the notion of a zero-point i.e. the location along the length of the channel where the surface potential is zero. The reason we established this was to ensure that for all surface charge densities, we could provide a reasonable volume fluid flow equation for various zero points.

Using a variety of zero-points we successfully provided a method to describe the volumetric flow through the channel using the Gouy-Chapman surface potential. We computed the Gouy-Chapman surface potential with a constant salt concentration and this gave us a linear volume flow-voltage diagram, however, we noted the non-linearity present in finite element calculations for positive electric potentials. We inspected the composition of the Gouy-Chapman surface potential equation. To incorporate the non-linearity present in the flow-voltage diagram for positive electric potentials, we computed the Debye length with the radially averaged salt concentration Eq. (3.14) instead of a constant salt concentration, that of the bulk. This approach was inspired by Ref. [45] where there was a discussion on how the Debye length varies with the salt concentration present within the system in question. A problem arose, to create the non-linear surface potential we were required to have a salt concentration which is dependent on the volumetric flow. This created a self-consistency issue which was solved by first implementing the linear equation with a constant Debye length of approximately 6.8nm into the radially averaged salt concentration. This provided us with a first iteration in volumetric flow and allowed us to continue with further iterations to enquire into the possibility of convergence in volume fluid flow. After eight iterations we found convergences in the flow for all zero-points. There were two cases where a full convergence occurred within two iterations, that of $x_0 = 0.3L$ and $x_0 = 0.4L$. Let's discuss why these two cases converged with fewer iterations by looking at the zero point $x_0 = 0.3L$. In Figure 10, we plotted the volumetric fluid flow as a function of the applied steady-state voltage. This system had a governing surface charge density of $e\sigma_0 = e\sigma_{ref} = 0.1e$ nm^{-2}. We noted that we had a good correlation for negative electric potentials but for positive voltages, we did not. This occurs as our analytical approximation for the radially averaged salt concentration does not operate to the same level of accuracy for a large surface charge density in positive electric potential regimes. This led us to investigate the optimal governing surface charge density. To reduce the governing surface charge density the salt concentration would not reach its minimal value for positive electric potentials. Therefore, we could capture the non-linearity present in the volume fluid flow to a higher degree of accuracy.

Reducing the governing surface charge density we found that we could capture the non-linearity of the volume flow to an improved agreement for $x_0 < 0.5L$ as depicted in Figure 11(b). There was a consistent intriguing result which occurred when the zero point was at $x_0 = 0.5L$, this was a constant zero flow. This result did not depend on the governing surface charge density. We saw that through the velocity streamlines the fluid would flow to the centre of the channel from both the tip and base and effectively annihilate regardless of the governing surface charge. We also inspected another velocity streamline case that of $x_0 = 0.7L$ and we found a contra-flow which reduces the overall flow when in the negative regime and aids in increasing the flow when in the positive electric potentials. This gave us further insight into the nature of these channels. We then looked into the effect of the flow on the salt concentration profiles. We could note a definite skewing occurring for the salt accumulations for negative electric potentials with less noticeable skewing negative voltages. For the finite element calculations result of the depletion this contrasted with the analytical result where it was very evident that the flow skewed the salt concentration for both positive and negative electric potentials. Moving back to the antisymmetric surface charge density present in $x_0 = 0.5L$ we found a perfectly parabolic salt concentration profile which we noted is the perfect environment for an annihilation of volumetric flow.

Continuing with a cylindrical channel we then investigated the diodic and Ohmic behaviour which occurs for certain charge densities along the channel walls. We found that to achieve diodic behaviour we are required to have some form of inhomogeneity present within the surface charge density equation. This meant that we were not necessarily required to have a bipolar channel. In the absence of inhomogeneity within the surface charge density we arrive at an Ohmic relation, i.e. a linear current-voltage relation. For the diodic case, we found a more apparent increase in conductivity for negative potentials, which is caused by the accumulation present within the channel. We noted that distilled water is an insulator by nature and when ions are placed within the fluid we increase the conductivity. Thus, by increasing the accumulation, the conductivity will also increase. We know that when we have a positive electric potential depletion occurs thus increasing the insulative nature of water, creating the plateau which we saw in Figure 16(a). This was an investigation purely for a steady state system, we moved then to a time-dependent study. This is where we proved analytically that cylindrical channels are capable of memristance. This was readily apparent via the pinched hysteresis loop.

In our final section, we researched conical channels. Our goal was to use the knowledge of volumetric flow and diodic behaviour acquired from the cylindrical channel and apply it to the conical channel. This would unify the theory for all geometries. We delved into the Ohmic and diodic nature of conical channels. We found that under certain conditions it is possible to remove the salt accumulation and depletion. It is the salt accumulation and depletion due to static electric potentials applied across the channel which create diodic behaviour. We came to learn that no matter the values used to create a bipolar conical channel diodic behaviour will always be produced. Similarly, if we have a homogeneous surface charge density we would also achieve diodic behaviour. However, in a very specific case of an inhomogeneous unipolar surface charge density we can achieve an Ohmic response. This Ohmic response removes the memristance from occurring in a time-dependent regime, as no accumulation or depletion occurs in the channel the current can flow with a constant linear conductivity.

Furthering our goal of applying the knowledge acquired from the cylindrical channel model, we shifted our attention to the volumetric flow of a conical channel. Previous research into similar channels by Ref. [18] required an effective surface potential to accurately model the flow along with the salt concentration. This influences other equations which are dependent on the salt concentration. We began our research into this issue by applying the laterally averaged Gouy-Chapman surface potential to understand the difference between finite element and analytical calculations. It appeared that the channel was weighted towards the tip. Thus, we weighed the zeta potential such that we could achieve a more correlated result to the finite element calculation for the linear volumetric flow. We found that weighing the cross-sectional area to the power $i = -4.5$ provided a reasonable approximation for the rotation observed by reducing the tip radius of the channel from $R_t = 200$ nm to $R_t = 50$ nm. Therefore, we applied the iterative method to this weighted function to no avail. This led us to purely focusing on the phenomenology present in the volumetric flow diagrams produced by FE analysis. We found that there is a noticeable pattern when we plotted the surface potential against the ratio of the base and tip radii. The diagram appears to converge for all zero points to a singular surface potential which informs us that the weight of the channel shifted to the base. As the charge density is assumed to be the same for all zero points at the base it makes intuitive sense that they would converge to a singular point. Lastly, we plotted the surface potential against the zero points, Figure 29, and fascinatingly, we found a purely linear graph.

While we purely delved into the phenomenological nature of the conical channel's volumetric flow. We considered the method we used to create the Gouy-Chapman zeta potential for the cylindrical channel. We were reminded that the Debye length varies with salt concentrations. Thus, we calculated the Debye length for its maximal and minimal value and found that the maximal approximate Debye length is 22 nm. This in turn affects the theory we were dealing with up to this point as we assumed that the radius of the channel to be much larger than the Debye length. Due to this, we must revert to the original equation for volumetric flow as we assumed that the second term present in Eq. (3.12) is negligible. It is worth noting that for the two terms in the aforementioned equation, we could achieve the plateauing effect due to both terms being of opposite signs.

As an outlook, we would like to investigate this final matter further to ensure that we can finally unify the full theory for any geometry used in iontronic devices. Another interesting aspect of iontronic devices which we would like to delve into further is the Onsager matrix which we hinted at being a 3×3 matrix seen in Eq. (2.36) for conical channels. This arises due to there being a possibility of creating a salt concentration difference across the channel. To the best of our knowledge it has only been evaluated in Ref. [46] where Werkhoven et al. computed all terms for a cylindrical channel. A 2×2 transport matrix was also computed for a conical channel, Ref. [3], which excluded the chemical difference in the channel. Moving to a different geometry will provide nuanced results with fascinating applications and further our understanding of transport in microfluidic channels.

References

[1] L. Bocquet. Nanofluidics coming of age. *Nat. Mater.*, **19**, 254, (2020).

[2] L. Bocquet and E. Charlaix. Nanofluidics, from bulk to interfaces. *Chemical Society Reviews*, **39**:1073–1095, (2010).

[3] W. Q. Boon, T. E. Veenstra, M. Dijkstra, and R. van Roij. Pressure-sensitive ion conduction in a conical channel: Optimal pressure and geometry. *Physics of Fluids*, **34**:101701, (2022).

[4] F. Caravelli and J. P. Carbajal. Memristors for the curious outsiders. *Technologies*, **6**, (2018).

[5] L. Chen, C. Yang, Y. Xiao, X. Yan, L. Hu, M. Eggersdorfer, D. Chen, D.A. Weitz, and F. Ye. Millifluidics, microfluidics, and nanofluidics: manipulating fluids at varying length scales. *Materials Today Nano*, **16**:100136, (2021).

[6] L. Chua. Memristor-the missing circuit element. *IEEE Transactions on Circuit Theory*, **18**:507–519, (1971).

[7] L. Chua. If it's pinched it's a memristor. *Semiconductor Science and Technology*, **29**, (2014).

[8] L. Chua and S. M. Kang. Memristive devices and systems. *Proceedings of the IEEE*, 64:209–223, (1976).

[9] H. Daiguji and Y. Oka et al. Nanofluidic diode and bipolar transistor. *Nano Letters*, **5**:2274–2280, (2005). PMID: 16277467.

[10] H. Davy. Additional experiments on galvanic electricity. *Nicholson's Journal of Natural Philosophy, Chemistry, and the Arts*, (1801).

[11] S. Dimitrijev. *Principles of Semiconductor Devices.* Oxford University Press, (2012).

[12] V.J. Francis. Fundamentals of discharge tube circuits. methuen's monographs on physical subjects. *Methuen*, (1948).

[13] H. Golnabi, M. Matloob, M. Bahar, and M. Sharifian. Investigation of electrical conductivity of different water liquids and electrolyte solutions. *Iranian Physical Journal*, **3**, (2009).

[14] Daniel G. Haywood, Anumita Saha-Shah, Lane A. Baker, and Stephen C. Jacobson. Fundamental studies of nanofluidics: Nanopores, nanochannels, and nanopipets. *Analytical Chemistry*, **87**(1):172–187, (2015).

[15] Y. He, D. Gillespie, and D. Boda et al. Tuning transport properties of nanofluidic devices with local charge inversion. *Journal of the American Chemical Society*, **131**:5194–5202, 2009. PMID: 19317490.

[16] L. Jubin, A. Poggioli, A. Siria, and L. Bocquet. Dramatic pressure-sensitive ion conduction in conical nanopores. *Proceedings of the National Academy of Sciences*, **115**:4063–4068, (2018).

[17] Iler R. K. *The chemistry of silica: solubility polymerization colloid and surface properties and biochemistry.* Wiley, (1979).

[18] T. M. Kamsma, W. Q. Boon, C. Spitoni, and R. van Roij. Unveiling the capabilities of bipolar conical channels in neuromorphic iontronics. *Faraday Discussions*, **246**:125–140, (2023).

[19] T. M. Kamsma, W. Q. Boon, T. ter Rele, C. Spitoni, and R. van Roij. Iontronic neuromorphic signaling with conical microfluidic memristors. *Physical Review Letters*, **130**, (2023).

[20] T. M. Kamsma, J. Kim, K. Kim, W. Q. Boon, C. Spitoni, J. Park, and R. van Roij. Brain-inspired computing with fluidic iontronic nanochannels, (2023).

[21] R. Karnik and K. Castelinoet et al. Diffusion-limited patterning of molecules in nanofluidic channels. *Nano Letters*, **6**:1735–1740, (2006). PMID: 16895365.

[22] M. L. Kovarik, K. Zhou, and S. C. Jacobson. Characterization of hepatitis b virus capsids by resistive-pulse sensing. *The Journal of Physical Chemistry B*, **113**, (2009).

[23] Michelle L. Kovarik, Kaimeng Zhou, and Stephen C. Jacobson. Effect of conical nanopore diameter on ion current rectification. *The Journal of Physical Chemistry B*, **113**(49):15960–15966, (2009).

[24] J. Leger, M. Berggren, and S. Carter. *Iontronics: Ionic Carriers in Organic Electronic Materials and Devices*, volume **1**. CRC Press, (2010).

[25] Yan Li, Dengchao Wang, Maksim M. Kvetny, Warren Brown, Juan Liu, and Gangli Wang. History-dependent ion transport through conical nanopipettes and the implications in energy conversion dynamics at nanoscale interfaces. *Chem. Sci.*, **6**:588, (2015).

[26] D. R. Lide. *CRC handbook of chemistry and physics*, (2004).

[27] V. S. Markin, A. G. Volkov, and L. Chua. An analytical model of memristors in plants. *Plant Signaling & Behavior*, **9**, (2014). PMID: 25482769.

[28] Brent Maundy, Ahmed S. Elwakil, and Costas Psychalinos. Correlation between the theory of lissajous figures and the generation of pinched hysteresis loops in nonlinear circuits. *IEEE Transactions on Circuits and Systems I: Regular Papers*, **66**:2606, (2019).

[29] Zheyi Meng, Yang Chen, Xiulin Li, Yanglei Xu, and Jin Zhai. Cooperative effect of ph-dependent ion transport within two symmetric-structured nanochannels. *ACS Applied Materials & Interfaces*, **7**(14):7709–7716, (2015).

[30] E. Mohamed, S. Josten, and F. Marlow. A purely ionic voltage effect soft triode. *Phys. Chem. Chem. Phys.*, **24**:8311–8320, (2022).

[31] Messr. Nicholson, Messr. Carlisle, and Messr. Cruickshank. Iv. experiments in galvanic electricity. *The Philosophical Magazine*, **7**:337–347, (1800).

[32] L. Onsager. Reciprocal relations in irreversible processes. i. *Phys. Rev.*, **37**:405–426, (1931).

[33] L. Onsager. Reciprocal relations in irreversible processes. ii. *Phys. Rev.*, **38**:2265–2279, (1931).

[34] S. Patankar. *Numerical Heat Transfer and Fluid Flow*, volume **1**. CRC Press, (1980).

[35] Gonçalo Paulo, Ke Sun, Giovanni Di Muccio, Alberto Gubbiotti, Blasco Morozzo della Rocca, Jia Geng, Giovanni Maglia, Mauro Chinappi, and Alberto Giacomello. Hydrophobically gated memristive nanopores for neuromorphic applications. *Nature Communications*, textbf14(1), (2023).

[36] A. Peters, S. L. Palay, and H. deF. Webster. *The fine structure of the nervous system: neurons and their supporting cells*, volume **3**. Oxford University Press, (1991).

[37] P. Robin, T. Emmerich, A. Ismail, A. Niguès, Y. You, G. H. Nam, A. Siria A. Keerthi, A. K. Geim, B. Radha, and L. Bocquet. Long-term memory and synapse-like dynamics in two-dimensional nanofluidic channels. *Science (New York, N.Y.)*, page 161–167, (2023).

[38] P. Robin, N. Kavokine, and L. Bocquet. Modeling of emergent memory and voltage spiking in ionic transport through angstrom-scale slits. *Science*, **373**(6555):687–691, (2021).

[39] Maheshwar Pd. Sah, Hyongsuk Kim, and Leon O. Chua. Brains are made of memristors. *IEEE Circuits and Systems Magazine*, **14**(1):12–36, (2014).

[40] V.K. Sangwan and M.C. Hersam. Neuromorphic nanoelectronic materials. *Nat. Nanotechnol.*, **15**:517–528, (2020).

[41] W. Shockley. The theory of p-n junctions in semiconductors and p-n junction transistors. *Bell System Technical Journal*, **28**:435–489, (1949).

[42] L. Squire, D. Berg, F. Bloom, S. du Lac, A. Ghosh, and N. Spitzer. *Fundamental Neuroscience*, volume 3rd ed. Academic Press, (2008).

[43] D. Strukov, G. Snider, and D. Stewart et al. The missing memristor found. *Nature*, page 80–83, (2008).

[44] H.W.F Sung and C. Rudowicz. Physics behind the magnetic hysteresis loop—a survey of misconceptions in magnetism literature. *Journal of Magnetism and Magnetic Materials*, **260**:250–260, (2003).

[45] R. van Roij. *Soft Condensed Matter Theory: 2020-2021*, Lecture Notes, Utrecht University (2021).

[46] B. L. Werkhoven and R. van Roij. Coupled water, charge and salt transport in heterogeneous nano-fluidic systems. *Soft Matter*, **16**:1527–1537, (2020).

[47] Wang X., Cheng C., Wang S., and Liu S. Electroosmotic pumps and their applications in microfluidic systems. *Microfluid Nanofluidics*, **6**, (2009).

A Appendix: Velocity Streamlines of Cylindrical Channel

In this section, we discuss the velocity streamlines of a cylindrical channel with two different inhomogeneous surface charge densities.

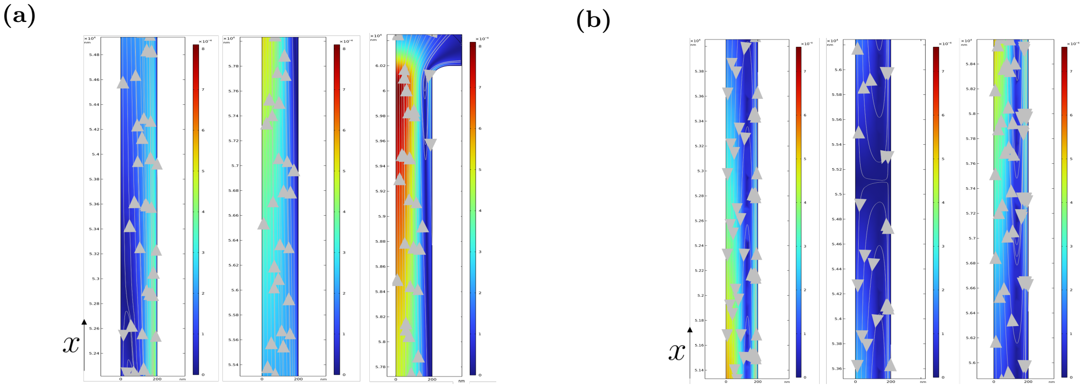

Figure 31: Velocity streamlines of cylindrical channels with varying zero points with the same governing surface charge $e\sigma_0 = 0.5e\sigma_{ref} = 0.05e$ nm^{-2}, the electric potential for these diagrams is $V = -0.2$ V. The colour bar represents the velocity of the fluid through the channel which appears as a heat map within the channel, and the arrows show the direction of fluid motion. Both channels are 200 nm in radius. **(a)** The zero-point of this channel is $x_0 = 0.7L$. **(b)** The zero-point of this channel is $x_0 = 0.5L$.

In Figure 31, we have depicted the velocity streamlines of channels with the zero-point $x_0 = 0.7L$, seen in Figure 31(a), and $x_0 = 0.5L$ seen in Figure 31(b). For the former channel, we can note that close to the tip of the channel there is a contra-flow occurring which diminishes approximately at $x = 0.7L$. However, this contra-flow does not become the dominant flow through the channel but merely dampens the overall flow through the channel. However when we move to a positive electric potential this contra-flow present in Figure 31(a) no longer works against the dominant flow. Therefore, we get an increase in flow which appears as a non-linear flow profile seen in 11(b) where there is a noticeable increase in flow.
Observing the second example of $x_0 = 0.5L$, the flow appears to move from the base to tip and tip to base with a similar velocity. When they meet at the centre of the channel the flows annihilate creating a situation where the flow through the channel is zero for all electric potentials. Indeed if we were to inspect the velocity stream lines for all electric potentials the same diagram is created. This shows the nature of the combination of perfect geometric symmetry and an antisymmetric surface charge density applied to the channel wall. This provides us with a useful visualisation of the fluid flow within the channels we have been researching.

B Appendix: 50nm Cylindrical Channel

We will now look at the flow profiles of a cylindrical channel with a radius of 50nm. The primary reason we are interested in this channel is to compare our results to that of a conical channel to deduce if indeed the Debye length being similar in length to the radius of the channel creates a situation where we cannot produce meaningful volumetric flow diagrams. To produce a meaningful computation we will set the governing surface charge density to be $e\sigma_0 = 0.5e\sigma_{ref} = 0.05e$ nm^{-2} to be comparable to our investigation of the 200nm cylindrical channel and conical channel we discussed in Section 5.3, along with the same constants described in Section 3.2.

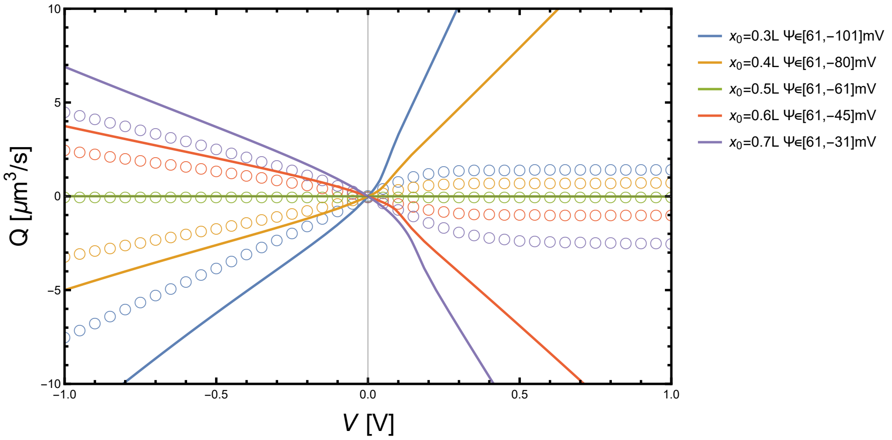

Figure 32: Volumetric flow as a function of an applied steady-state electric potential V. Computed for a cylindrical channel of radius $R = 50$ nm with governing surface charge density $e\sigma_0 = 0.5e\sigma_{ref} = 0.05e$ nm^{-2}. We vary the zero point of the surface charge density $\sigma(x)$ to be in the range $x_0 \in [0.3L, 0.7L]$ increasing in increments of $0.1L$.

In Figure 32 we plot the volumetric flow against the static electric potential. We note that our analytical solution breaks down similarly to the conical channel seen in Section 5.3. There is a plateau effect occurring for the positive electric potential regime and our method used to compute the volumetric flow for the cylinder with a radius of 200 nm no longer works even after several iterations. It is now apparent that as discussed previously our Debye length is no longer much smaller than the radius of the channel. Therefore, we must refer back to the equation which we derive, Eq. (3.12). Here we ignored the second term as we assumed $\lambda_D \ll R$. By analysing the Debye length that is calculated using a varying salt concentration we can note that this is no longer true and in essence, we approach $\lambda_D \approx R/2$.

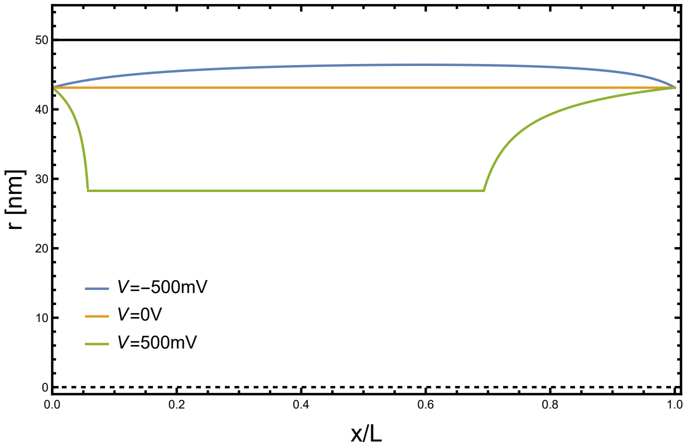

Figure 33: The analytically approximated Debye length along the length of a 50 nm cylindrical bipolar channel for varying static electric potentials denoted by the coloured solid lines. The governing charge density is $e\sigma_0 = 0.5e\sigma_{ref}$ where the zero point in this case is $x_0 = 0.7L$. The black dotted line signifies the centre of the cylindrical channel and the solid black line is the channel wall, the coloured lines denote the Debye length displayed by plotting $R - \lambda_D(x, V)$.

In Figure 33, we plot the analytically approximated Debye length along the channel length for varying static electric potentials ranging from $V = [-500, 500]$ mV. We depicted the centre of the channel with a black dotted line and the channel wall is located at $r = 50$ nm. In this case, the governing surface charge density is $e\sigma_0 = 0.5e\sigma_{ref}$ and the zero point is located at $x_0 = 0.7L$. We observe the implementation of the minimal salt concentration present in the system as the Debye length levels off to a constant value of approximately 22 nm. We undoubtedly are no longer in the assumed regime of $\lambda_D \ll R$.